3D printed NdFeB permanent magnets by laser powder bed fusion: process feasibility, optimization and annealing

Yong Rong Chan and Sankaranarayanan Seetharaman
Department of Additive Manufacturing Industrialisation Group, Advanced Remanufacturing and Technology Centre, Singapore, Singapore, and
Jerry Y.H. Fuh and Heow Pueh Lee
Department of Mechanical Engineering, National University of Singapore, Singapore, Singapore

Graphical Abstract

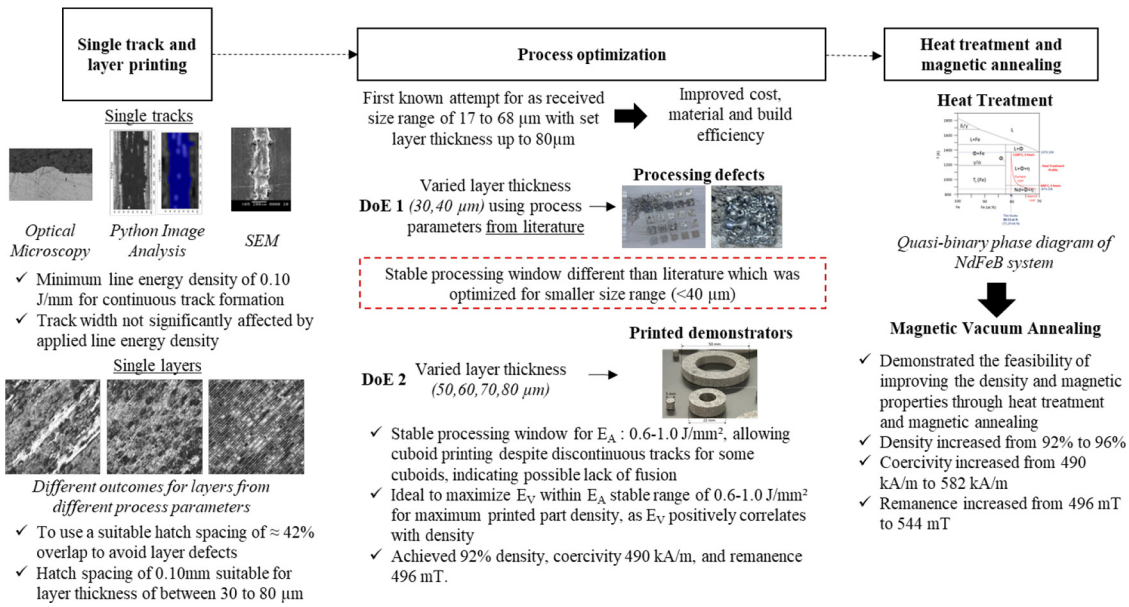

Abstract

Purpose – This study aims to assess the feasibility of laser powder bed fusion (LPBF) processing using as-received gas-atomized spherical Neodymium-Iron-Boron (NdFeB) powder (17–68 μm), compared to literature methods that sieve to a narrow size range (<40 μm).

Design/methodology/approach – The research involves single track and layer printing, process optimization and subsequent heat treatment and magnetic annealing. The experimental approach includes conducting systematic printing trials to assess the impact of various parameters on printed track and layer quality, and refining printing parameters through iterative testing. Heat treatment and magnetic annealing are applied to achieve the desired magnetic properties.

Findings – A minimum linear energy density of 0.10 J/mm is required for continuous track formation, with track width largely unaffected by varying linear energy densities. An optimal hatch spacing of approximately 42% overlap avoids layer defects, with 0.10 mm spacing suitable for layer thicknesses between 30 and 80 μm. A stable processing window for energy density (EA) of 0.6–1.0 J/mm^2 was identified, allowing cuboid printing despite some discontinuous tracks, indicating potential fusion issues. Maximizing volumetric energy density (EV) within this range correlates positively with part density, achieving 92% density, coercivity of 490 kA/m and remanence of 496 mT. Post-treatment, density increased to 96%, coercivity to 582 kA/m and remanence to 544 mT.

The current issue and full text archive of this journal is available on Emerald Insight at: **https://www.emerald.com/insight/1355-2546.htm**

Rapid Prototyping Journal
31/6 (2025) 1118–1140

[DOI 10.1108/RPJ-07-2024-0278]

Received 6 July 2024
Revised 20 November 2024
Accepted 6 January 2025

Originality/value – This study fills a significant gap in LPBF literature for NdFeB by using the original wider size range of spherical powder without sieving, demonstrating improved cost-effectiveness, material efficiency and build efficiency. These findings offer practical recommendations for addressing the challenges related to LPBF processing of NdFeB powder.

Keywords Permanent magnets, NdFeB, Laser powder bed fusion, Process optimization, Design of experiments, Sustainability

Paper type Research paper

1. Introduction

There exists incredible potential to improve the efficiency of electrical machines through design optimization of magnetic parts by tapping on to the advantages offered by 3D printing (3DP) which include enhanced design freedom, rapid prototyping, reduced material wastage and reduction to supply chain cost. In particular, the 3DP of permanent magnets (PM) is of particular interest as it helps to realize near-net complex-shaped PM with strong and reliable magnetic fields for better performance and energy efficiency (Ferretti, 2017; Huijuan Liu, 2019; Yong and Lu, 2003).

Among various types, Neodymium-Iron-Boron (NdFeB) magnet offers unique magnetic properties like high coercivity and high magnetic field strength relative to their size and hence it is widely used in several applications (Honshima and Ohashi, 1994; Stopic and Friedrich, 2021). However, there are challenges associated with high raw material cost and supply chain issues. Here, it is important to consider laser powder bed fusion (LPBF) as it has the potential to achieve better densification and feature resolution among several additive manufacturing (AM) processes. In this aspect, pioneers in the field like (Jacimovic *et al.*, 2017), (Kolb *et al.*, 2016) and (Bittner *et al.*, 2020) have successfully demonstrated superior coercivity (H_c) and remanence (B_r) for LPBF printed NdFeB compared to injection moulded and spark plasma sintered counterparts (Jaćim *et al.*, 2017; Rafal Wrobel, 2019). However, there are limited information available in the open literature pertaining to the process parameters applicable for LPBF processing of NdFeB PM.

LPBF is advantageous over other AM processes for fabricating magnets due to its high precision and control over complex geometries and microstructures. Unlike processes such as Binder Jetting or fused deposition modeling, LPBF offers superior control of material properties through selective melting and solidification, which is crucial for optimizing magnetic performance (Yu *et al.*, 2022). Additionally, LPBF allows for high energy densities that are essential for fully consolidating magnetic powders like NdFeB, resulting in better mechanical properties and improved magnetic strength. This process also enables near-net-shape fabrication, reducing material waste and post-processing requirements, making it highly efficient for manufacturing custom and intricate magnet designs (Buhairi *et al.*, 2022).

Currently, the supply chain of NdFeB powder for 3DP is limited to only one type (Magnequench) with a fixed size range (17–68 μm), as primarily determined by centrifugal atomization, the method for producing NdFeB powder. In this regard, the published literatures (Vock *et al.*, 2019) highlights the fact that the current practice adhered for LPBF processing of NdFeB requires sieving the virgin powder to less than 45 μm which is uncommon compared to other virgin metal powders of similar size range for LPBF processing. However, it is not very clear if the powder sieving is indeed necessary prior to printing and whether it brings additional benefits or drawbacks in terms of material wastage. One thing which is clear is that the sieving process actually leads to excessive wastage of powder feedstock and excess material cost to meet the powder volume requirements.

While few notable research works have stated that a finer, homogenous powder does bring potential benefits in terms of improved printability and feature resolution (Franke *et al.*, 2016; Goll *et al.*, 2021; Liu *et al.*, 2011), the process of sieving away the undesired powder particles is not ideal given the resource scarcity and geopolitical issues associated with rare earth metals like Nd. For example, (Bittner *et al.*, 2020) reported having sieved the as-received powder at a size close to the median size of the as-received powder size spectrum. In doing so, while median refers to the value in the middle of a data set, this means that approx. 50% of the entire would have been sieved away in the process. Where only 50% of the as-received powder is used, a build requiring 40 kg of feedstock powder would require the user to purchase twice the required amount at 80 kg, so that the as-received powder can be sieved down to the finer size range used. Further, it is also important to consider the benefits of including larger sized particles that are beneficial in terms of cost, safety and particle-size effect during oxidation (El-Sayegh *et al.*, 2020; Mellin *et al.*, 2016).

In view of the above-mentioned research gaps, an attempt is made in this research work to investigate the feasibility of using the entire size range of as-received NdFeB powder through the optimization of LPBF process parameters. For this purpose, an extensive design of experiments (DoE) was carried out assessing the outcome in terms of the porosity of printed parts vs energy input.

In LPBF processing, the energy inputs can be represented in different ways such as liner energy density (E_L), area energy density (E_A) or volumetric energy density (E_V) which can be calculated from the process variables using the following equations (equation (1)–(3) (Bittner *et al.*, 2021), (Buhairi *et al.*, 2022):

$$\text{Linear Energy Density}, E_L = \frac{P}{v} \tag{1}$$

$$\text{Area Energy Density}, E_A = \frac{P}{v \times d} \tag{2}$$

$$\text{Volumetric Energy Density}, E_V = \frac{P}{v \times d \times T_L} \tag{3}$$

where P, ν, d and T_L respectively denote the laser power in watts, scan speed in mm/s, scan spacing in mm and layer thickness in mm.

(Bittner *et al.*, 2021) considered E_A as the key variable for the LPBF processing of NdFeB and found that E_A between 0.8–2.3 J/mm^2 can produce stable builds while $E_A < 0.6$–0.8 J/mm^2 was inefficient to melt the powder particles and results in highly porous samples. Similarly, the delamination was reported as increased when E_A is more than 2.3 J/mm^2. The same group also

found that the choice of power, scan velocity and hatch spacing had minor importance, if AED lies within 0.8–2.3 J/mm^2 (Bittner *et al.*, 2020). However, there are no clear findings relating the effects of layer thickness, (i.e. volumetric energy density input) as the research works on LPBF processing of NdFeB PM are just emerging with most of the works demonstrating the printing of MQP-S powder using different commercial LPBF machines (Bittner *et al.*, 2020; Bittner *et al.*, 2021; Emminghaus *et al.*, 2020; Franke *et al.*, 2016; Huber *et al.*, 2019; Jaćim Jaćimović, 2017; Jacimovic *et al.*, 2020; Urban *et al.*, 2017a, 2017b, 2017c; Wu *et al.*, 2021) while a few attempted to improve magnetic performance through the optimization of laser power parameters (Bittner *et al.*, 2020; Franke *et al.*, 2016), grain boundary infiltration (Urban *et al.*, 2017a, 2017b, 2017c) and laser exposure strategy (Urban *et al.*, 2017a, 2017b, 2017c).

Therefore, in this study, to assess the feasibility of using the entire size range of as-received NdFeB powder in the LPBF process, the process parameters were optimized in two phases considering both the area and the volumetric energy densities. In the first phase, the relationship between E_A density values and the build outcome by varying processing parameters was studied. In the second phase, the effect of volumetric energy density on the outcome of the build was assessed by varying the volumetric energy density for a fixed area density.

The printed NdFeB sample with the highest density obtained in this study undergoes heat treatment to enhance both its density and magnetic properties. Following heat treatment, the samples are subjected to magnetic vacuum annealing in a specialized magnetic vacuum annealing oven (MVAO). This process not only further enhances the magnetic properties but also crucially aligns the magnetic dipoles to provide the magnet with a specific direction. To the best of our knowledge, the use of magnetic vacuum annealing for LPBF processed magnets has never been attempted before. This directional alignment is essential for the functional application of LPBF-processed magnets in practical, real-world scenarios.

2. Methodology

In this study, two differentiated strategies were set: characterizing the NdFeB powder feedstock and optimizing the LPBF process. First, the powder's particle size and shape distribution were analyzed using microscopy. Second, the feasibility and optimization of LPBF were explored through systematic experiments. Initial trials focused on energy densities ranging from 0.5–7.5 J/mm^2 to print single tracks and layers, while subsequent optimization varied laser power and layer thickness to enhance part density and magnetic properties.

The energy density range from 0.5–7.5 J/mm^2 was selected based on both theoretical considerations and experimental optimization from previous studies on LPBF processes for metal-based materials, including NdFeB (Buhairi *et al.*, 2022; Caiazzo *et al.*, 2020; Yu *et al.*, 2022). The lower limit of 0.5 J/mm^2 ensures sufficient energy input to initiate the melting process without causing excessive porosity, while the upper limit of 7.5 J/mm^2 prevents overheating, which can lead to material degradation and undesirable phase changes in NdFeB. This range was chosen to explore and balance optimal fusion, densification and magnetic property retention in the printed magnets. Additionally, these values align with literature data on energy densities used in LPBF processing of metal powders with similar thermal properties (Caiazzo *et al.*, 2020). A wider range was implemented especially considering that literature reported stable processing window of the NdFeB powder was at a much smaller size range (<40 μm) when compared to the as-received powder size range used in this study (17–68 μm).

The study achieved significant improvements in density, coercivity and remanence through precise parameter control, heat treatment and magnet vacuum annealing, demonstrating the feasibility of producing high-quality NdFeB magnets with enhanced performance.

3. Experimental approach

3.1 Material selection

In this research, the chosen material was a centrifugally atomized bonded NdFeB magnetic powder (MQP-S-11–9 - 20001), sourced from NeoMagnequech, China. NdFeB is a high-performance magnetic material known for its superior magnetic properties, which include high coercivity and remanence.

3.1.1 Specimen preparation

3.1.1.1 Hot mounting. The preparation of samples for microscopy analysis was conducted using a standardized mounting and polishing protocol to ensure accurate and reproducible results. The samples were mounted with the cross-section of the tracks facing downward and held upright using a "SamplKlip," a specialized plastic specimen holder designed to maintain precise alignment during the mounting process. The hot mounting procedure was performed under controlled conditions with a heat time of 2 min, cooling time of 4 min, applied pressure of 290 bars and a temperature of 180 °C. These parameters were selected based on the resin's thermal and mechanical properties and the equipment manufacturer's recommendations, tailored to ensure proper encapsulation of the sample while minimizing thermal and mechanical stresses. In addition, reference to literature found that the equipment manufacturer's recommendations were similar to findings in literature (Echlin, 2011; Ravikumar *et al.*, 2014):

- Heating

A heating duration of 2 min was sufficient to achieve complete polymerization of the mounting resin. This parameter ensures uniform flow of the resin around the sample, avoiding insufficient coverage or uneven encapsulation. Moreover, limiting the heat exposure mitigates potential microstructural changes in temperature-sensitive sample materials, particularly those with low thermal stability:

- Cooling

The cooling phase was optimized to prevent the development of residual stresses within the resin and sample. Rapid cooling could introduce microcracks or distortion at the resin-sample interface due to uneven shrinkage. The controlled cooling time ensures gradual solidification, promoting a robust bond between the resin and the sample:

- Pressure

The applied pressure (of 290 bars) was applied to enhance resin infiltration into fine features of the tracks while avoiding deformation of the sample. This level of pressure ensures complete encapsulation, preventing the formation of voids or

gaps that could compromise the integrity of the mounted sample:

- Temperature

The curing temperature (of 180 °C) was set to match the resin's glass transition and curing requirements, promoting optimal flow and adhesion. The temperature was also calibrated to prevent thermal damage to the sample material, ensuring that the original microstructure remained unaltered.

3.1.1.2 Polishing procedure. Mounted samples were subjected to a sequential polishing process using abrasives of progressively finer grit sizes. This procedure was designed to achieve a smooth, defect-free cross-section while preserving the structural features of the sample. The polished surfaces were examined to ensure the absence of preparation-induced defects, such as scratches or artifacts.

The selected parameters for hot mounting and polishing were optimized to balance the physical and thermal requirements of the resin and the material properties of the sample. The controlled heat and pressure facilitated resin flow around the intricate features of the tracks, while the gradual cooling minimized internal stresses. The polishing process further ensured that the exposed cross-sections were free of artifacts, enabling high-resolution microscopy analysis. The preparation process produced 12 hot-mounted and polished specimens, each containing 240 tracks. The stepwise results of the preparation are shown in Figure 1.

3.1.1.3 Heat treatment and magnetic annealing specimens. Post-printing, selected specimens underwent heat treatment to improve magnetic properties. The heat treatment plan involved sintering at 1100 °C, furnace cooling to 600 °C and quench cooling. This was similarly done by (Brown *et al.*, 2002) through conventional powder metallurgy of NdFeB where heating was carried out at 1100 °C for a few hours (unspecified duration). (Fukuno *et al.*, 1990) and (Yan *et al.*, 2011) have similarly used a similar sequence for powder metallurgy for magnet processing where the powder was sintered, followed by heat treatment. The suggested temperature and durations were generally similar and yielded positive outcomes with regards to improving magnetic performance (Fukuno *et al.*, 1990; Yan *et al.*, 2011). Specimens were then treated in a MVAO oven at 350 °C for four hours to align magnetic dipoles and establish the magnet's north and south poles.

3.2 Characterization of NdFeB powder

Centrifugal atomized bonded NdFeB magnetic powder (MQP-S-11–9 - 20001 or simply MQP-S) from "NeoMagnequech, China" was used as the raw material. The particle size and shape distribution of the powder was assessed as per the standard test methods/established procedures as described below.

3.2.1 Particle size and shape distribution

An automated microscope "model - Morphologi G3" from Malvern Panalytical" was used to measure the particle size and shape distribution of the MQP-S powder. The methodology involves dispersing a fine quantity of powder onto the measurement platform using compressed air followed by automatic image capturing of powder particles with a light microscope and then evaluation of their individual size and shape. A total of 36,000 particles were assessed, and the results were averaged.

3.3 Laser powder bed fusion processing of NdFeB powder

3.3.1 Single tracks and layers

A Concept Laser M2 Cusing Multilaser Metal AM System was used for the printing of NdFeB powder in this study. The parameters and their ranges are as follows: layer thickness from 30 to 80 μm (in increments of 10), laser power from 50 to 150 W (in increments of 25) and from 200 to 400 W (in increments of 50), scan speed from 750 to 1500 mm/s (in increments of 250) and a fixed hatch spacing of 0.1 mm. The process parameter range was determined with reference to existing literature on the LPBF of NdFeB and other material types used for LPBF (Buhairi *et al.*, 2022; Chan *et al.*, 2024; Watring *et al.*, 2020) Notably, the reported processing ranges in these studies were based on powders sieved to particle sizes of 32 μm (Kolb *et al.*, 2016; Urban *et al.*, 2017a, 2017b, 2017c) and 40 μm (Bittner *et al.*, 2020; Bittner *et al.*, 2021). The studies highlighted a stable processing window for laser power between 10 and 150 W, with laser powers above 200 W reported to cause process instability (Bittner *et al.*, 2020). While the current study used powders with a significantly different size distribution (17–68 μm) and characteristics, these previously reported ranges provided a critical baseline for parameter selection, ensuring a balance between process stability and material integrity.

In this study, a total of 240 tracks were generated, each with a unique set of process parameters. By systematically varying these parameters, the study aimed to identify optimal settings that produce continuous, well-defined tracks with minimal defects. The process began with the creation of an STL file, designed using dedicated data and build preparation software. This was followed by the utilization of parameter definition software, which enabled the precise input and assignment of the desired process parameters for each respective track. This structured approach ensures thorough exploration of the parameter space and facilitates the identification of conditions that yield high-quality tracks.

In addition, single layers were also printed to assess effect of hatch spacing on the printing of a layer of NdFeB using printer's (Concept Laser M2 Cusing) default island scan strategy which was originally designed to alleviate the thermally induced residual stresses during printing (Chen *et al.*, 2021; Cheng *et al.*, 2016; Kruth *et al.*, 2010; Yasa *et al.*, 2009). The parameters and their ranges are as follows: layer thickness from 40 to 70 μm (in increments of 10), laser power from 80 to 120 W (in increments of 20), scan speed from 200 to 1200 mm/s (in increments of 200) and a varying hatch spacing from 0.06–0.14 mm. This yields a total of 216 squares with unique sets of process parameters. The coupons were printed using the default island scan strategy to alleviate thermally induced residual stresses (Chen *et al.*, 2021; Cheng *et al.*, 2016; Kruth *et al.*, 2010; Yasa *et al.*, 2009).

3.3.2 Design of experiments

This exploratory study to develop a stable processing parameter range for as-received MQP-S NdFeB powder was conducted in two phases:

Figure 1 Mounting and polishing of samples for microscopy analysis

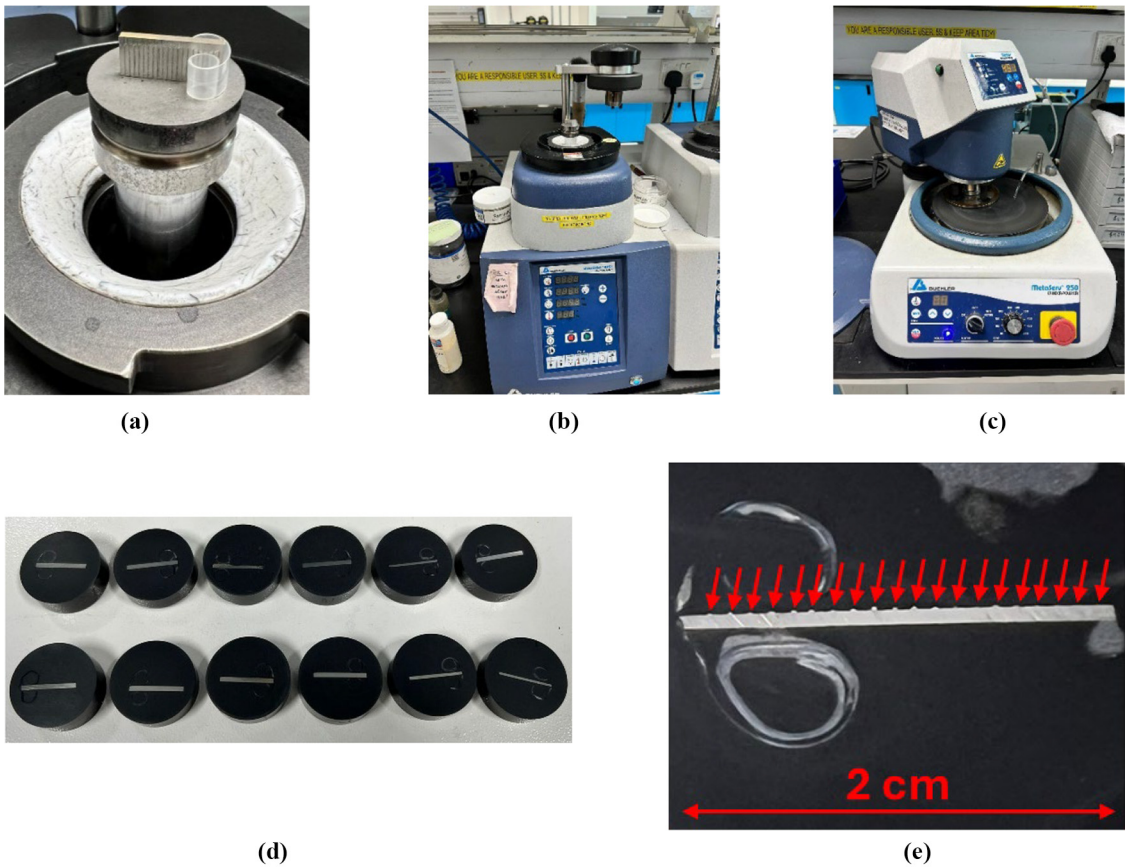

Notes: (a) Mounting of sample with cross-section of track facing down, held upright using "SamplKlip", a plastic specimen support clip; (b) hot mounting with heat time of 2 min, cool time of 4 min, with applied pressure of 290 bars at 180 °C; (c) Polishing of samples with; (d) Hot mounted polished samples: 12 coupons with exposed cross-section of a total of 240 tracks; (e) Visually obvious tracks after polishing, illustrated with red arrows
Source: Figure by authors

Phase 1: As shown in Figure 2, the first phase of the study investigated the processability of un-sieved NdFeB powder using energy densities between 0.5 and 7.5 J/mm^2. In this phase, a total of 50 cubes were printed in two separate batches, each batch having fixed layer thicknesses of either 30 or 40 μm. The parameters varied during this phase included laser power, scan speed and hatch spacing, with ranges between 500 and 150 W for laser power, 100–1500 mm/s for scan speed and 0.02–0.10 mm for hatch spacing. This phase aimed to establish a broad understanding of how these variables impact the print quality and the processability of the NdFeB powder. The results from this phase were crucial for identifying the initial parameter sets that could be further refined. The detailed summary of the parameters tested can be found in Table 1, while the list of process parameter sets evaluated for the printing of non-sieved NdFeB during DOE Phase II can be found in Table 2.

Figure 2 DOE Phase 1 using literature values for sieved condition <40 μm

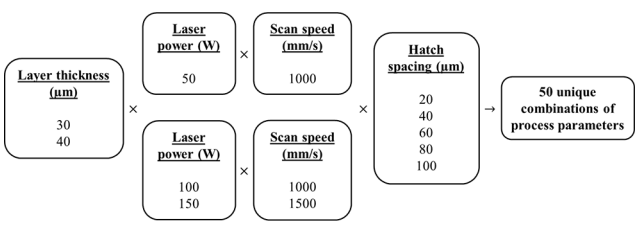

Source: Figure by authors

Phase 2: The second phase focused on further optimizing the process parameters (as shown in Figure 3) based on the findings from Phase 1. This phase involved varying the laser power between 50 and 140 W and adjusting the layer thickness between 50 and 80 μm. The scan speed and hatch spacing were kept constant at 1000 mm/s and 0.1 mm, respectively. The goal during this phase was to maintain an energy density between 0.5 and 1.4 J/mm^2, adjusted in increments of 0.1 J/mm^2. The primary objective was to achieve the highest possible part density and optimal magnetic properties by fine-tuning these parameters. This systematic approach aimed to identify the most effective combination of settings for producing high-quality, high-density NdFeB parts with superior magnetic performance.

Table 1 List of process parameter sets evaluated for the printing of non-sieved NdFeB during DOE Phase I

S/N	Layer thickness (mm)	Laser power (W)	Scan speed (mm/s)	Hatch spacing (mm)	Area energy density (J/mm^2)	Volumetric energy density (J/mm^3)
1.01	0.03	50	1000	0.02	2.5	83.3
1.02				0.04	1.3	41.7
1.03				0.06	0.8	27.8
1.04				0.08	0.6	20.8
1.05				0.10	0.5	16.7
1.06		100	1000	0.02	5	166.7
1.07				0.04	2.5	83.3
1.08				0.06	1.7	55.6
1.09				0.08	1.3	41.7
1.10				0.10	1	33.3
1.11			1500	0.02	3.3	111.1
1.12				0.04	1.7	55.6
1.13				0.06	1.1	37
1.14				0.08	0.8	27.8
1.15				0.10	0.7	22.2
1.16		150	1000	0.02	7.5	250
1.17				0.04	3.8	125
1.18				0.06	2.5	83.3
1.19				0.08	1.9	62.5
1.20				0.10	1.5	50
1.21			1500	0.02	5	166.7
1.22				0.04	2.5	83.3
1.23				0.06	1.7	55.6
1.24				0.08	1.3	41.7
1.25				0.10	1	33.3
2.01	0.04	50	1000	0.02	2.5	62.5
2.02				0.04	1.3	31.3
2.03				0.06	0.8	20.8
2.04				0.08	0.6	15.6
2.05				0.10	0.5	12.5
2.06		100	1000	0.02	5	125
2.07				0.04	2.5	62.5
2.08				0.06	1.7	41.7
2.09				0.08	1.3	31.3
2.10				0.10	1	25
2.11			1500	0.02	3.3	83.3
2.12				0.04	1.7	41.7
2.13				0.06	1.1	27.8
2.14				0.08	0.8	20.8
2.15				0.10	0.7	16.7
2.16		150	1000	0.02	7.5	187.5
2.17				0.04	3.8	93.8
2.18				0.06	2.5	62.5
2.19				0.08	1.9	46.9
2.20				0.10	1.5	37.5
2.21			1500	0.02	5	125
2.22				0.04	2.5	62.5
2.23				0.06	1.7	41.7
2.24				0.08	1.3	31.3
2.25				0.1	1	25

Source: Table by authors

Table 2 List of process parameter sets evaluated for the printing of non-sieved NdFeB during DOE Phase II

S/N	Layer thickness (mm)	Laser power (W)	Scan speed (mm/s)	Hatch spacing (mm)	Area energy density (J/mm^2)	Volumetric energy density (J/mm^3)
3.01	0.05	50	1000	0.1	0.5	10
3.02		60			0.6	12
3.03		70			0.7	14
3.04		80			0.8	16
3.05		90			0.9	18
3.06		100			1	20
3.07		110			1.1	22
3.08		120			1.2	24
3.09		130			1.3	26
3.10		140			1.4	28
4.01	0.06	50	1000	0.1	0.5	8.3
4.02		60			0.6	10
4.03		70			0.7	11.7
4.04		80			0.8	13.3
4.05		90			0.9	15
4.06		100			1	16.7
4.07		110			1.1	18.3
4.08		120			1.2	20
4.09		130			1.3	21.7
4.10		140			1.4	23.3
5.01	0.07	50	1000	0.1	0.5	7.1
5.02		60			0.6	8.6
5.03		70			0.7	10
5.04		80			0.8	11.4
5.05		90			0.9	12.9
5.06		100			1	14.3
5.07		110			1.1	15.7
5.08		120			1.2	17.1
5.09		130			1.3	18.6
5.10		140			1.4	20
6.01	0.08	50	1000	0.1	0.5	6.3
6.02		60			0.6	7.5
6.03		70			0.7	8.8
6.04		80			0.8	10
6.05		90			0.9	11.3
6.06		100			1	12.5
6.07		110			1.1	13.8
6.08		120			1.2	15
6.09		130			1.3	16.3
6.10		140			1.4	17.5

Source: Table by authors

Figure 3 DOE Phase 2 testing wider layer thickness settings

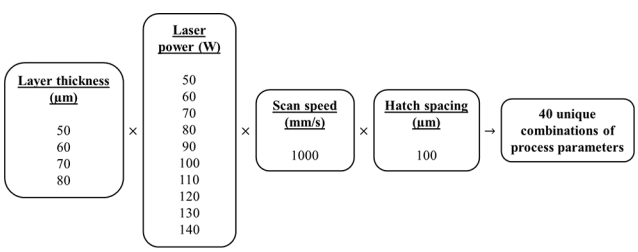

Source: Figure by authors

3.4 Characterization of laser powder bed fusion-processed samples

3.4.1 Properties of single tracks and layers

3.4.1.1 Sem. A "JEOL JSM-5600LV" SEM was used to study the tracks; to identify the microstructural features and type of defects for selected samples. SEM can reveal detailed morphological features, such as voids, cracks, surface roughness and particle distributions, enabling a thorough assessment of defect types and their underlying causes.

3.4.1.2 Microscope. The Olympus BX53M microscope is used to measure the NdFeB single tracks by providing high-

resolution imaging and precise measurement capabilities. This instrument allows for detailed observation of the track morphology, width and continuity, which are critical for assessing the quality of the printed tracks.

3.4.1.3 Image processing using python to measure single track properties. First, an image of the LPBF tracks is loaded using the OpenCV library. This image is read into the program from the file of interest (for example, named "test2.tif"). The image is initially in color (BGR format), and the first step in processing is to convert it to grayscale. This conversion simplifies the image data, making it easier to work with in subsequent steps.

Next, to reduce noise and improve edge detection, a Gaussian blur is applied to the grayscale image. The Gaussian blur smooths the image by averaging the pixel values with their neighbors, which helps in minimizing the impact of noise. After blurring, the Canny edge detection algorithm is used to identify the edges in the image. This algorithm detects a wide range of edges in the blurred grayscale image by looking for areas of rapid intensity change.

To further smooth the detected edges and reduce noise, another Gaussian blur is applied to the edge-detected image. This additional blurring helps in refining the edges and preparing the image for contour detection. At this point, the original image, the edge-detected image and the blurred edge-detected image are displayed using Matplotlib to visually confirm the effectiveness of the edge detection and smoothing processes, as illustrated in Figure 4 below.

To measure the width of the track, the mask is analyzed column by column, as shown in Figure 5. For each column, the number of non-zero (white) pixels is counted, which represents the track width in that column. These width values are collected into an array and converted to actual measurements using a scaling factor (in this case, 0.2558). A sample result for the thickness of a track, in terms of pixel count" is illustrated in Figure 5(e). It is noteworthy that the manual method of using the image analysis software which accompanies the optical microscope is susceptible to human error. For the same track measured, it is observed that the average is somewhere instead at approximately 200 μm., as illustrated in Figure 5(f) below.

This was much larger than the actual thickness which is more accurately measured using Python. The sample size obtained by Python is as many pixels as available in the horizontal direction (in this study, 5,000 points), where in manual methods, it can be limited to much fewer points due to feasibility of the means of data collection (around 10–15 points per track). The width data is then analyzed to understand the distribution of the track widths. This methodology provides a systematic approach to measuring the width of LPBF tracks using image processing, ensuring accurate and reliable results that can be used to assess the quality and consistency of the AM process. In a similar way, the cross-section of the tracks (as illustrated in Figure 6 below) were also measured using Python.

Figure 4 Conversion from original image to "edge detected image", to "edge detected blurred image" with shown values in scale of axis in terms of pixel count

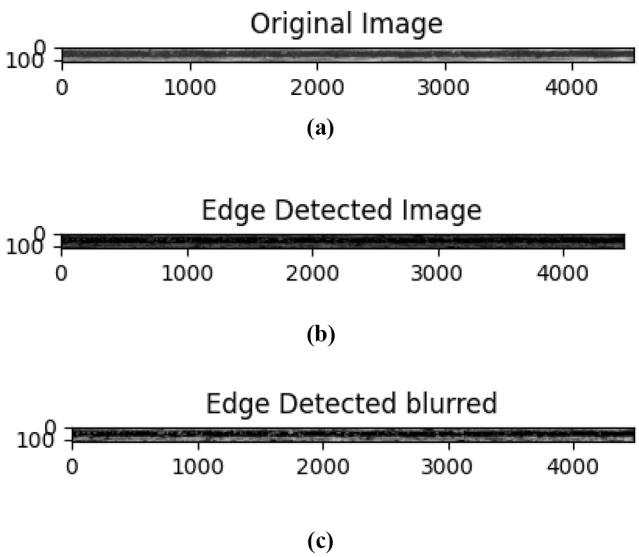

Notes: (a) Original; (b) Processed for edge detection; (c) Processed for edge detection with blur
Source: Figure by authors

3.4.2 Density of 3D-geometries (cuboids)

The test specimens that cleared visual check were wire cut and then subjected to Archimedes' density measurements for relative density using equation (4), as per ASTM B311 using a Sartorius Secura224-1S Analytical Balance from "Mettler Toledo and ethanol as the liquid medium:

$$\text{Relative Density, } \rho = \frac{m_a}{(m_a - m_f}\, x\, (\rho_f - \rho_a) + \rho_a \qquad (4)$$

where m_a = mass in air; m_f = mass in fluid; ρ_a = density of air; and ρ_f = density of fluid.

3.4.3 Magnetic property

The magnetic properties of the feedstock NdFeB powder and the NdFeB magnets (processed through LPBF) were assessed using a Superconducting Quantum Interference Device Vibrating Sample Magnetometer (SQUID-VSM). The powder sample quantity used for measurement was kept at 50 mg and the solid samples' volume was approx. 1–2 mm^3 with a mass of approximately 8 mg. Coercivity measurements derived from hysteresis loop analysis were completed at a set temperature of 300 K (room temperature setting).

3.5 Post-processing of laser powder bed fusion-processed samples

3.5.1 Heat treatment

Understanding the importance of achieving a maximum amount of the $Nd_2Fe_{14}B$ (Φ) phase, we attempted at devising an approach for heat treatment. To the best of our knowledge, there are no reported TTT diagrams for NdFeB, therefore we have instead made reference to the available quasi-binary phase diagram (QBPD) of the NdFeB system (Filip *et al.*, 2005) for the purposes of deciding on the temperatures to be set for the heat treatment of the NdFeB specimen. To refer to the QBPD of NdFeB (Filip *et al.*, 2005), we required to understand the Fe atomic percent which was a derivative of its weight percent. The weight percent measurement of 71.23% was obtained through chemical composition analysis using standards CAP-017S (ICP-AES) and ASTM E 1019–18 (Combustion/IGF). Through conversion, we

Figure 5 Conversion from original image to "largest black patch" with shown values in scale of axis in terms of pixel count

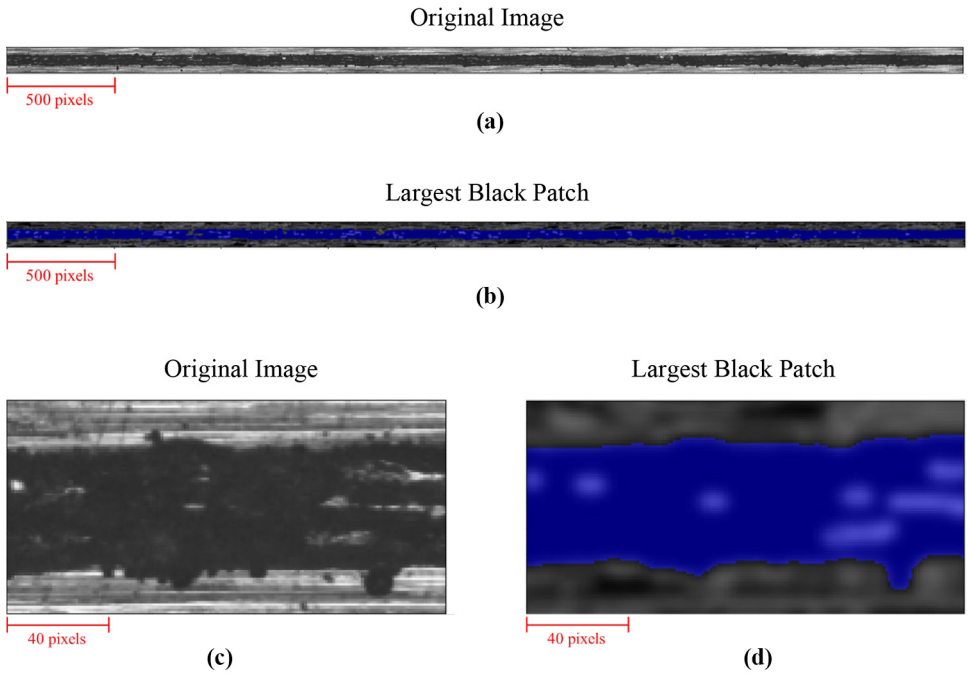

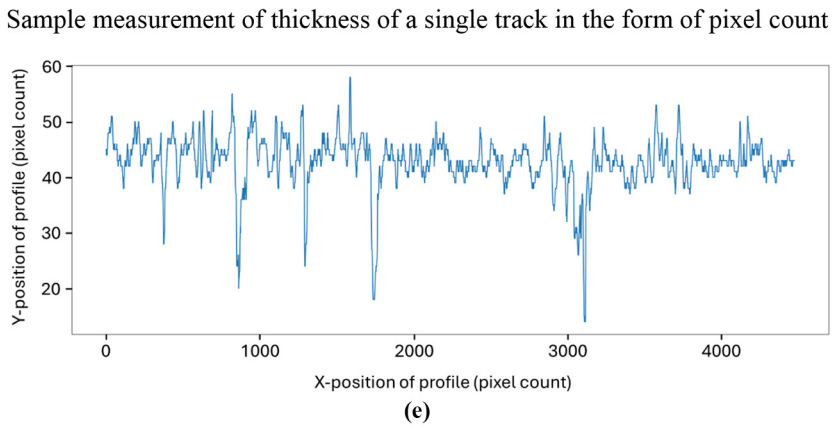

(e)

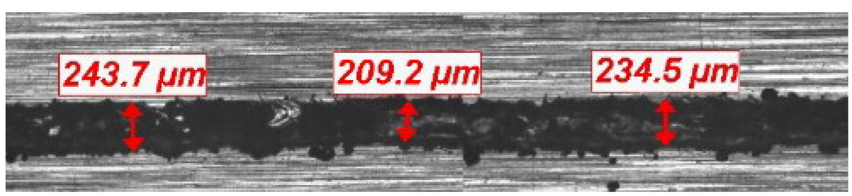

(f)

Notes: (a) Original; (b) Processed; (c) Original – Magnified; (d) Processed – Magnified; (e) Sample measurement of thickness of a single track in the form of pixel count; (f) Illustration of track measurement using conventional manual methods via image analysis software (inaccurate when verified using Python – pixel counting method)
Source: Figure by authors

Figure 6 Microscopy image of cross-section

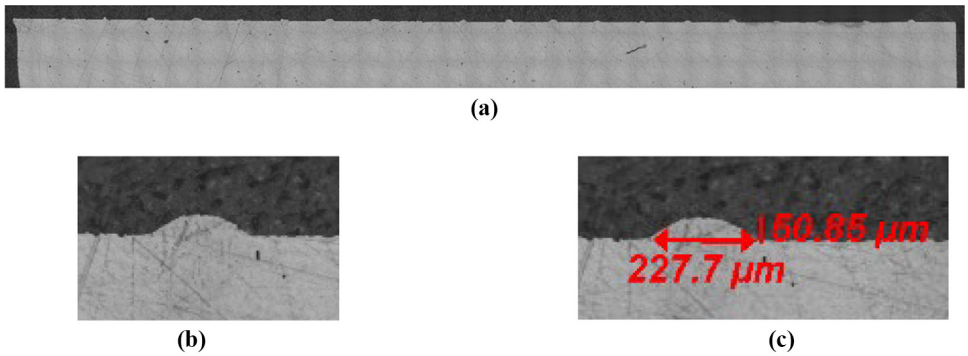

Notes: (a) Merged image; (b) Close-up of cross-section of a single track; (c) Close-up of cross-section of a single track with manually assigned dimensions, which was not used as the method for measurement due to human error, since image processing using Python through pixel count was a viable option
Source: Figure by authors

have found the atomic percent to be 80.52% and indicated it in Figure 7 below.

3.5.2 Magnet vacuum annealing
Magnet vacuum annealing was conducted in a MVAO by "Futek Furnace" of model "SFM-13-2T-NV". It has a maximum temperature of 500 °C and normal temperature (standard or ambient temperature conditions under which experiments or operations are conducted) of 300 °C. In this study, the magnet was annealed in the MVAO for 4 h at 350°C.

4. Results and discussion

4.1 Characteristics of NdFeB powder

4.1.1 Particle size and shape distribution
Figure 8 shows the results of particle size and shape analyses performed using Morphologi G3. It reveals circle equivalent (C.E.) in the range between 17 μm (D_{10}) and 68 μm (D_{90}) with median size at 40 μm (D_{50}). With respect to shape, the particle's shape factor as characterized by high sensitivity (HS) circularity indicates that the powder is generally of good sphericity with a mean value at 0.95 where the value of 1.00 is indicative of a perfectly circular sphere. These results were in good agreement with other studies where the powder shape was confirmed as mostly spherical with minimal satellites through SEM imaging (Bittner *et al.*, 2020; Emminghaus *et al.*, 2020; Wu *et al.*, 2021).

4.2 Outcome of laser powder bed fusion processing single tracks and layers

It was observed that continuous tracks could be achieved for all layer thickness settings used and different layer thickness used result in different outcomes for tracks when the other process parameters were kept constant (as shown in Figure 9).

Upon investigation, it was observed that a minimum applied energy density was required to ensure adhesion and fusion onto the build plate. Generally, it was observed that a minimum E_L of 0.10 J/mm is required to print a continuous track. Upon comparison between coupons "A1" and "F1" from Figure 9(c) above, it was observed that varying outcomes were observed while considering that the only difference between these two

Figure 7 Heat treatment plan in this study, with reference made to quasi-binary phase diagram of the NdFeB system (Filip *et al.*, 2005)

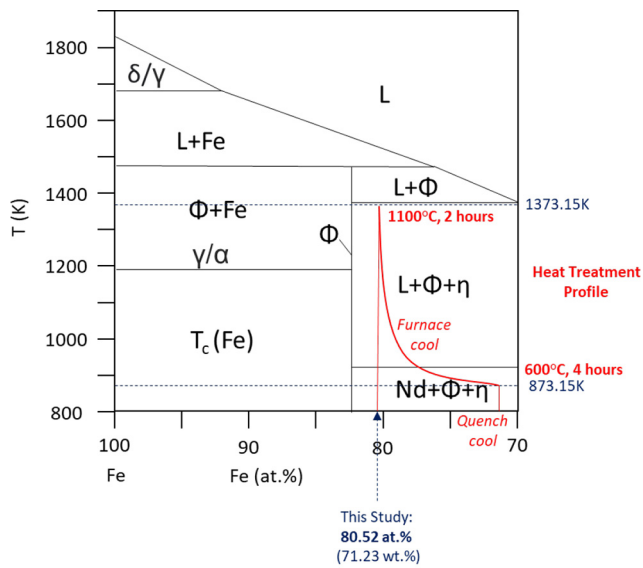

Source: Figure courtesy of Filip *et al.*, 2005

are the set layer thicknesses, at 30 and 80 μm respectively. As illustrated in Figure 9(d)–(e), it was observed that linear energy density of 0.13 J/mm did not yield a continuous line for when set layer thicknesses of 80 μm was used, unlike the case for set layer thicknesses of 30 μm.

As illustrated in Figure 10(f) below, at high laser power settings, it was also observed that some tracks were partially discontinuous with high variations of track width, suggesting less repeatability with higher variation of track outcome. This discontinuity could also be attributed to poor powder spreadability where insufficient powder was deposited on the build plate for complete sintering of the entire track. This hypothesis stems from the set layer thickness of 40 μm, being the same as the median size of NdFeB feedstock powder being

Figure 8 Results of particle size and shape analyses from morphologi G3

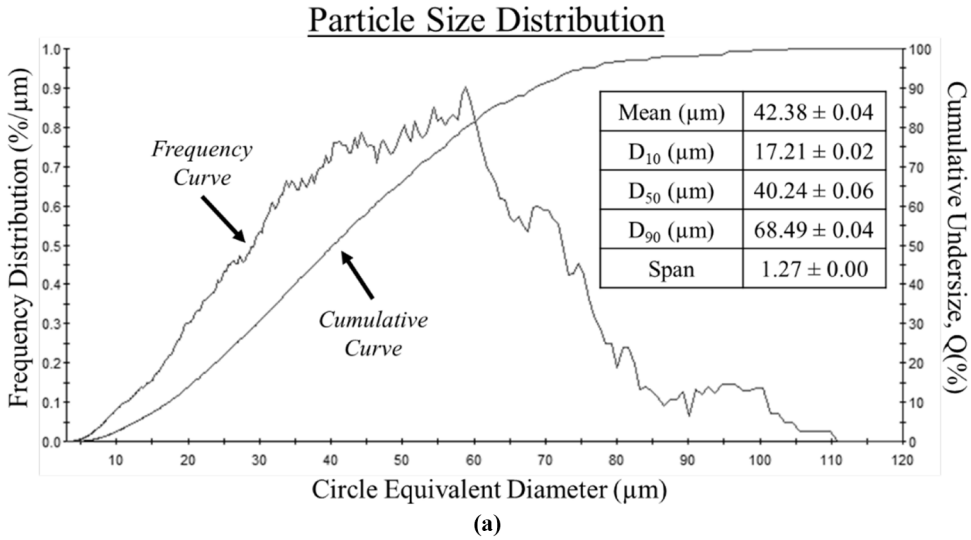

(a)

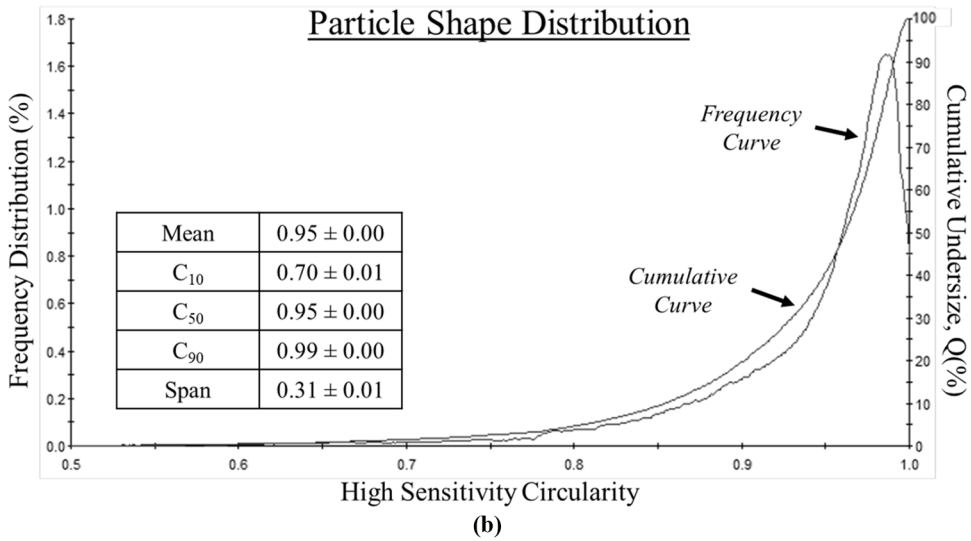

(b)

Notes: (a) Circle equivalent (CE) particle size distribution; (b) High sensitivity (HS) Circularity distribution
Source: Figure by authors

used. This suggests that only 50% of the powder can deposit effectively on the build plate under the set layer thickness of 40 μm, while the other 50% of the powder larger than 40 μm will be pushed to the overflow. Through SEM imaging, it was also observed that balling occurred in cases where there was high laser powder and low scan speed, causing excessive heat input, as shown in Figure 9(g)–(h) above.

In this study, we have measured the width of the tracks in two ways, one from top view microscopy and the other from the cross-section of the track. It was found that the cross-section measurement was more accurate when validated against SEM images. Cross-sectional views are less affected by surface artifacts like balling and spattering, which can distort width measurements in top-view microscopy. As illustrated in Figure 10(f) below, it was observed that the difference between the two measurements can range from approximately 100–200 μm. The other graphs in Figure 10 below illustrate the relationships between linear energy density and the dimensions (width and height) of tracks, measured from both top-view and cross-sectional perspectives.

Understanding the correlation between linear energy density, track width and height informs optimal hatch spacing in LPBF processes. Appropriate hatch spacing ensures adequate overlap between tracks, enhancing bonding and reducing defects such as porosity or lack of fusion, as shown in Figure 11.

Incomplete melting as seen in Figure 11(c) above, can cause defects like porosity and lack of fusion, which compromise the

Figure 9 Wire-cut coupons with printed tracks of varying processing parameters and set layer thicknesses

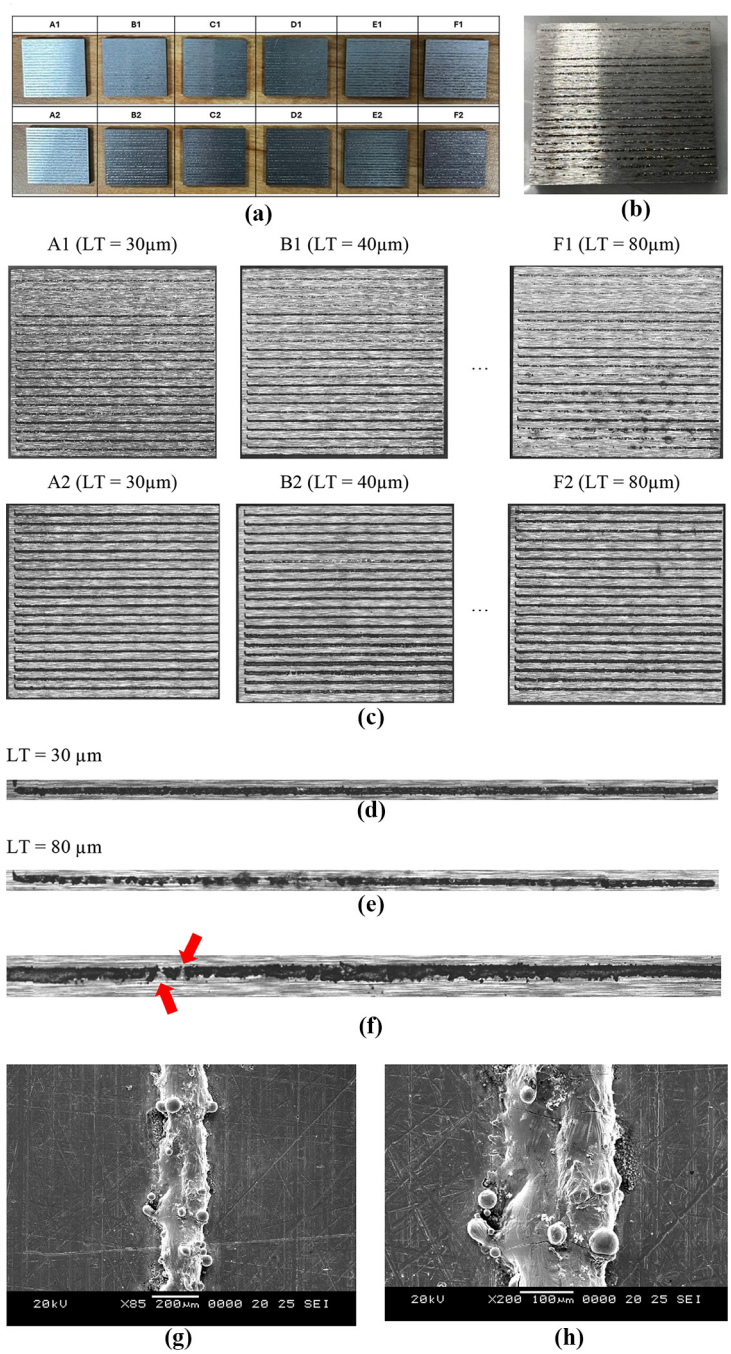

Notes: (a) Overview of all 12 square coupons with 20 tracks on each coupon; (b) close-up view of a coupon, showing visually obvious defective tracks; (c) representative microscopy images of the coupons to illustrate that continuous tracks can be printed on all layer thickness settings from 30 μm to 80 μm; (d)–(e) difference in outcome of track with the same applied linear energy density and different set layer thickness; (f) non-continuous track at high laser power of 400 W at scan speed of 1000 mm/s with layer thickness of 40 μm (with red arrows indicating points of discontinuity); (g)–(h) SEM images of track with occurrence of balling: (g) magnification of 85x; (h) magnification of 200x
Source: Figure by authors

structural integrity and mechanical properties of the 3D printed part. Ensuring optimal hatch spacing, is essential to achieve complete melting, uniform layer deposition and strong inter-track bonding, thereby improving the overall quality and reliability of the printed part. On the other hand, it was observed in Figure 11(a) that a hatch spacing too close together have caused surface defects of balling to occur, likely due to the higher resultant E_A.

For the case of Figure 11(b), good overlapping of tracks was observed at hatch spacing of 0.10 mm when measured track width (measured from cross-section) was approximately 0.17 mm (166.75 μm). Considering equation (5) below, we measure the percentage overlap to be approximately 42% (within the industry-known suggested overlap of 30% to 50%):

$$Percentage\ Overlap = \frac{Track\ width - Hatch\ spacing}{Track\ width} \quad (5)$$

It is noteworthy that considering that the width of the tracks did not vary much when compared against applied E_L, it may

Figure 10 Correlation obtained only from the continuous tracks printed (146 out of 240 tracks)

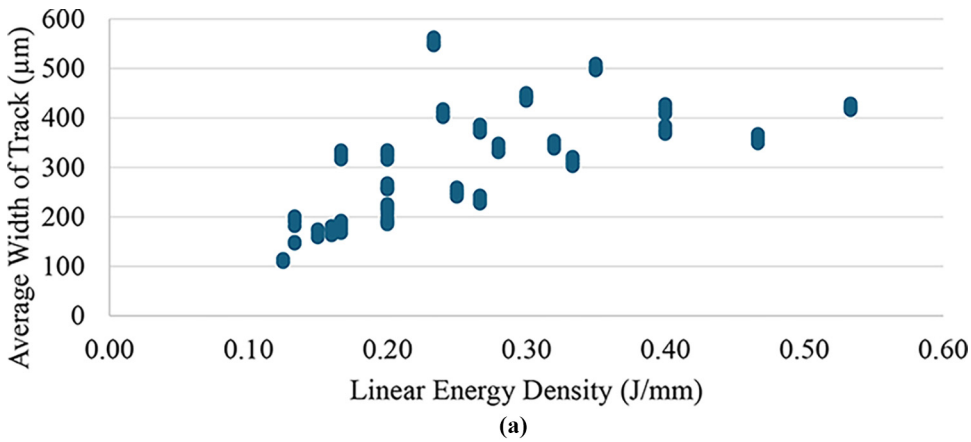

(a)

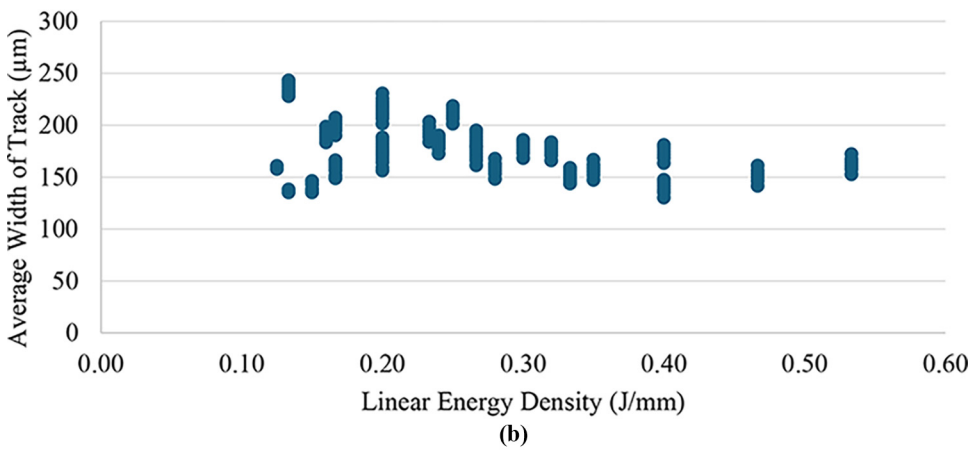

(b)

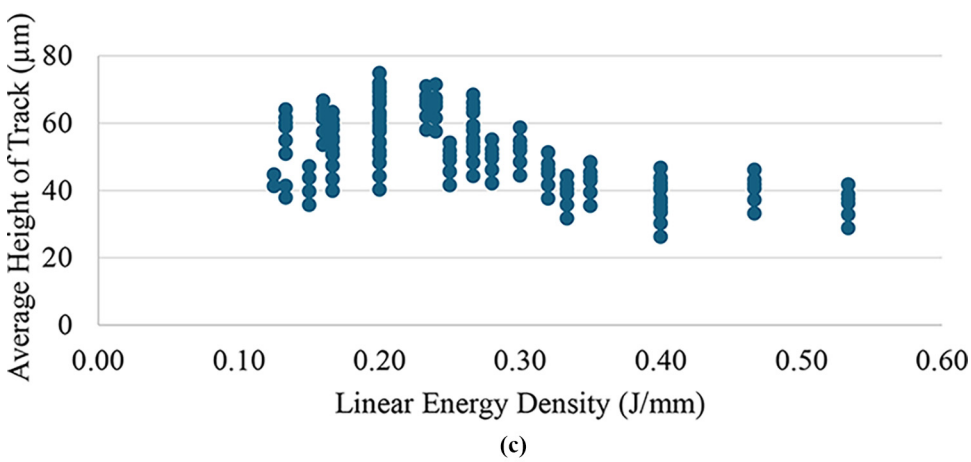

(c)

(*continued*)

Figure 10

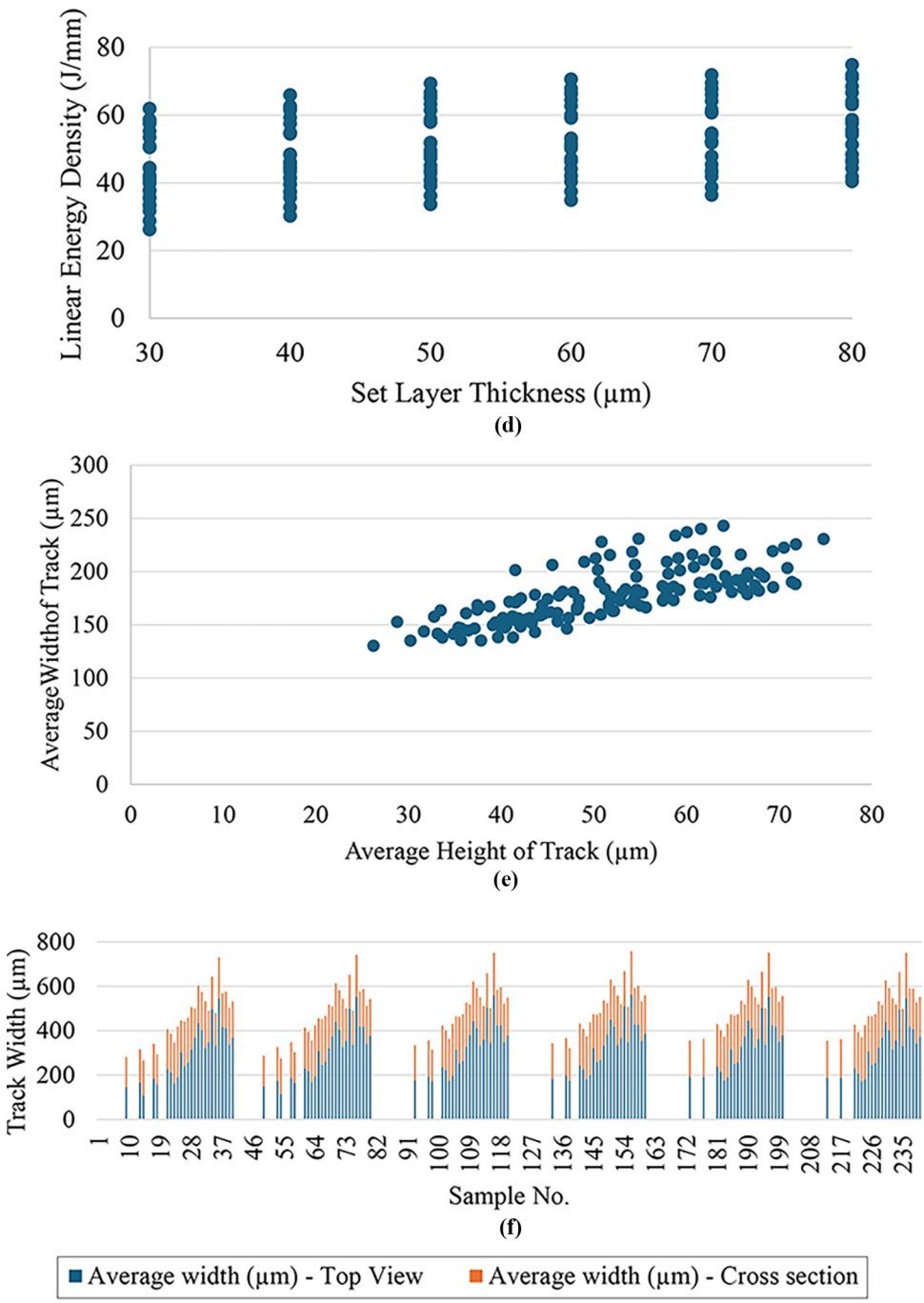

Notes: (a) Correlation between linear energy density and width of track, measured from top-view; (b) Correlation between linear energy density and width of track, measured from cross-sectional view; (c) Correlation between linear energy density and height of track, measured from cross-sectional view; (d) Correlation between set layer thickness and height of track, measured from cross-sectional view; (f) Comparison between top-view and cross-sectional view measurement of track width

Source: Figure by authors

Figure 11 Different print outcomes when varying hatch spacing while keeping other parameters constant LT = 70 μm, laser power = 100 W, scan speed = 1000 mm/s

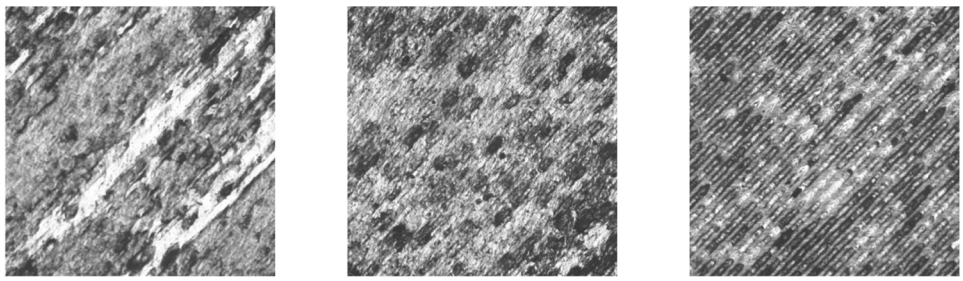

(a) (b) (c)

Notes: (a) Hatch spacing = 0.06 mm; (b) Hatch spacing = 0.10 mm; (a) Hatch spacing = 0.14 mm
Source: Figure by authors

Figure 12 Outcome of phase I DoE for the printing of non-sieved NdFeB MQP-S powder showing

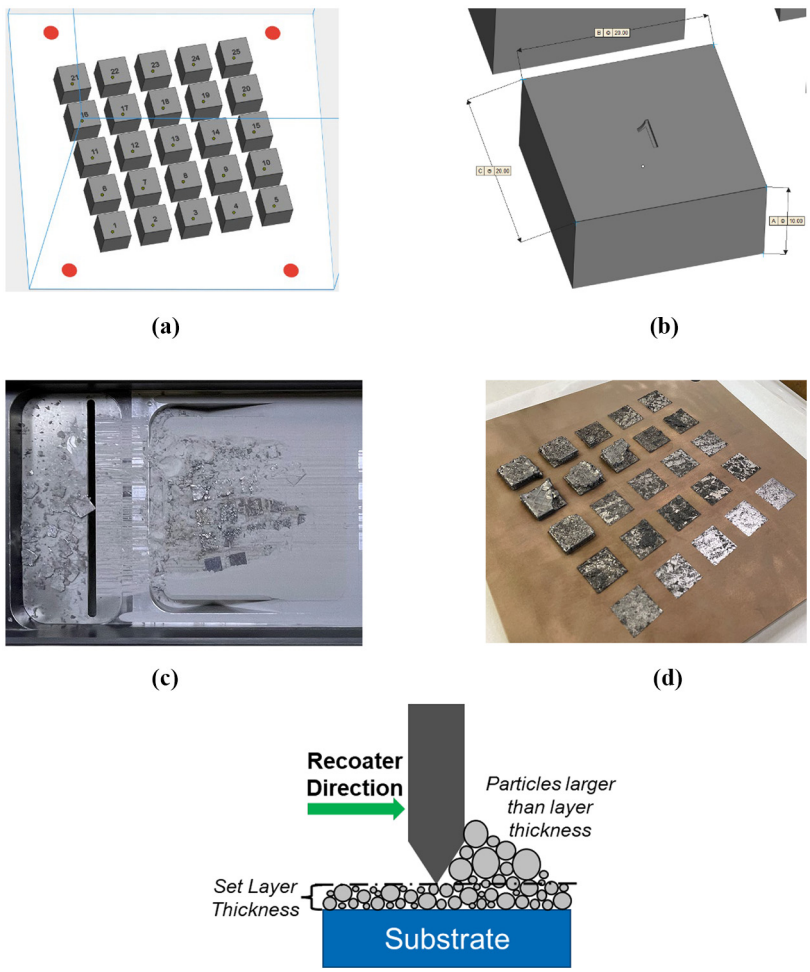

(a) (b) (c) (d) (e)

Notes: (a) CAD file; (b) Close-up with dimensions of CAD for one cube; (c) The streak line defects during the spreading of powder, (d) Delamination of printed cubes from the build plate and (e) Mechanism of preferential segregation of particles larger than set layer thickness
Source: Figure by authors

suggest that the minimum hatch spacing, and percentage overlap is universal for all settings for the LPBF of NdFeB.

This section on single track and layer LPBF-processing of NdFeB concludes two key factors to consider when deciding upon process parameters;

- To have a minimum E_L of 0.10 J/mm for continuous track formation.
- To use a suitable hatch spacing of ≈ 42% overlap to avoid layer defects.
- Track width not significantly affected by applied E_L, therefore hatch spacing of 0.10 mm is suitable for layer thickness of between 30 and 80 μm.

4.3 Optimization of laser powder bed fusion processing of 3D geometries

For the 30 μm layer thickness build, severe recoating defects were observed during the printing process as shown in Figure 12(a)–(b) which could have been caused by particles that are significantly larger than the set layer thickness. Further, the printed parts also suffered significant delamination even though the energy density used in this DoE (0.8 and 2.3 J/mm^2) was well within the range reported by other researchers (Bittner *et al.*, 2020), the only difference being the PSD due to non-sieving. Hence, the failure of prints in DoE-1 can be surely attributed to the difference in PSD. With a significant difference between the set layer thickness

Figure 13 Outcome of 40 μm layer thickness build showing

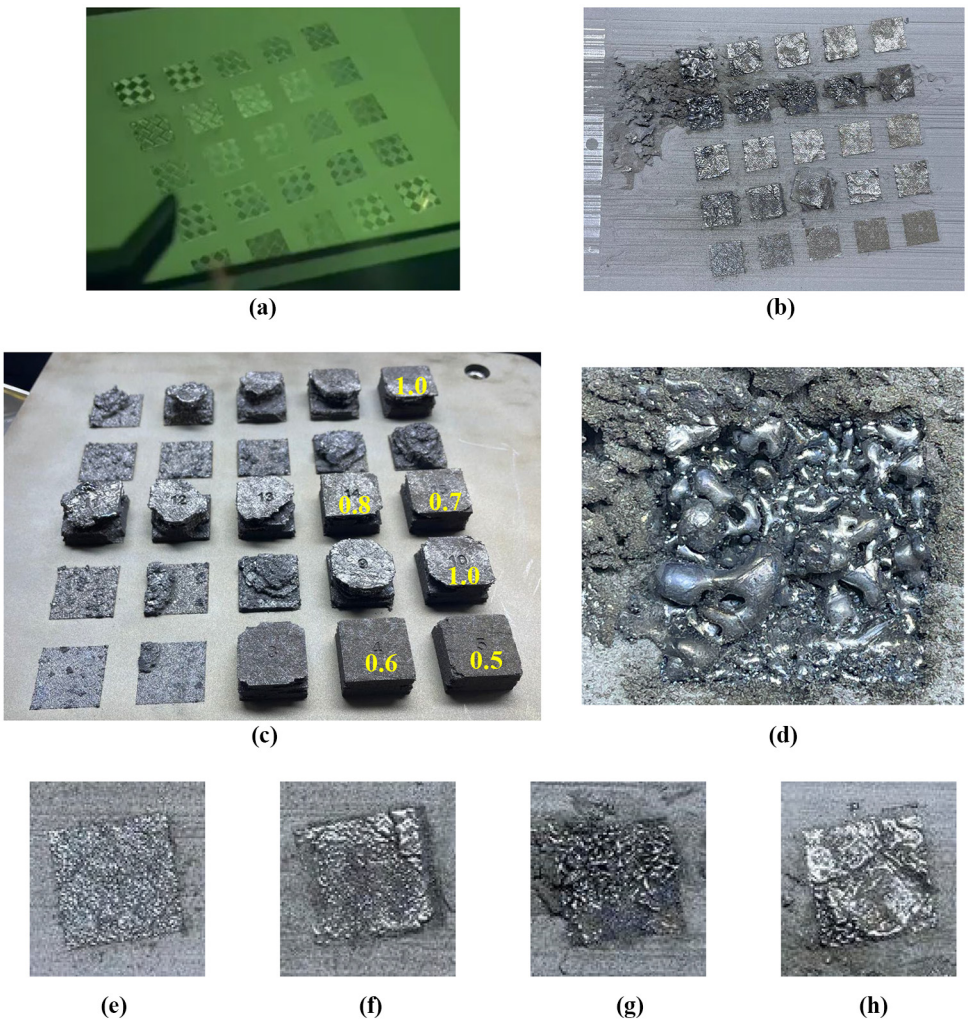

Notes: (a) Stable printing during the first few layers; (b)–(c) Few defective coupons in the build after the completion of printing process, where coupons with EA between 0.5 and 1.0 J/mm2 are labelled with their EA value; (d) Evaporation of molten metal characterised by molten-like appearance, where image was captured after build was completed but did not hold after removing of build as seen in parts; (b)–(c) of this figure; (e)–(h) Different print outcomes from the same energy density with different contributing process parameters, where images were taken before build was removed from the LPBF printer; (e) Laser Power (LP) = 50 W, Scan Speed (SS) = 1000 mm/s, Hatch Spacing (HS) =0.02; (f) LP = 100 W, SS = 1000 mm/2, HS = 0.04 mm; (g) LP = 150 W, SS = 1000 mm/2, HS = 0.06mm; (h) LP = 150 W, SS = 1500 mm/2, HS = 0.04 mm
Source: Figure by authors

(30 μm) and the size range of the powder particles (17–68 μm, with a median size of 40 μm), the recoater would push away a reasonable quantity of powder particles with size larger than the layer thickness from the build plate into the overflow chamber. The potential mechanism is described in Figure 13(e). This hence leads to insufficient powder volume on the build plate resulting in uneven energy absorption and print failure.

For the 40 μm layer thickness, while the first few layers exhibited good quality with effective bonding with the build plate as shown in Figure 14(a), defects appeared toward the end of the build as shown in Figure 14(b)–(c) although the overall quality of the build is significantly better with several successfully built coupons compared to the previous build printed using 30 μm layer thickness. These observations clearly highlight the fact that the area density window (0.8 and 2.3 J/mm^2) as suggested in the literature (Bittner *et al.*, 2020) is not completely suitable if the powder un-sieved (as-received) MQP-S NdFeB powder is directly used for printing. Further, it is also important to note that delamination between layers have occurred when the energy density was above 1.3 J/mm^2. Similarly, the evaporation of molten metal (as characterized by poor solidification and molten-like appearance) was observed for energy density, $E_A \geq 1.9$ J/mm^2 as shown in Figure 14(d).

Through the outcome of these two prints with reference to the area energy densities of the printed cubes, it is found that the stable processing window suggested in literature [between 0.8 and 2.3 J/mm^2 (Bittner *et al.*, 2020)] is not suitable when the powder is not sieved to a finer size range of less than 40 μm prior to LPBF processing.

With reference to the area energy densities of the cubes which have printed successfully as shown in Figure 15(c), a processing window which results in stable prints for cubes is derived to exist between 0.5 and 1.0 J/mm^2. When comparing cubes printed at the same area and volumetric energy density, it is observed that different contributing process parameters (Laser Power, Scan Speed and Hatch Spacing) will result in different print results, as shown in Figure 15(e)–(h). Figure 16 below shows the outcome of DoE Phase 2 wherein majority of the coupons were printed successfully, while a few cubes printed using larger area energy density (E_A) displayed defects.

First, the quality of the prints has sufficiently improved by increasing the layer thickness from 30 to 50 μm as defects such as cracks and delamination were less prominent for E_A less than 1.0 J/mm^2. However, visual checks did not reveal any substantial improvements for layer thickness above 50 μm, thus suggesting 50 μm as the critical layer thickness for the given particle size distribution, 17–68 μm. Second, the delamination as occurred in

Figure 14 Printed cubes in Phase 2

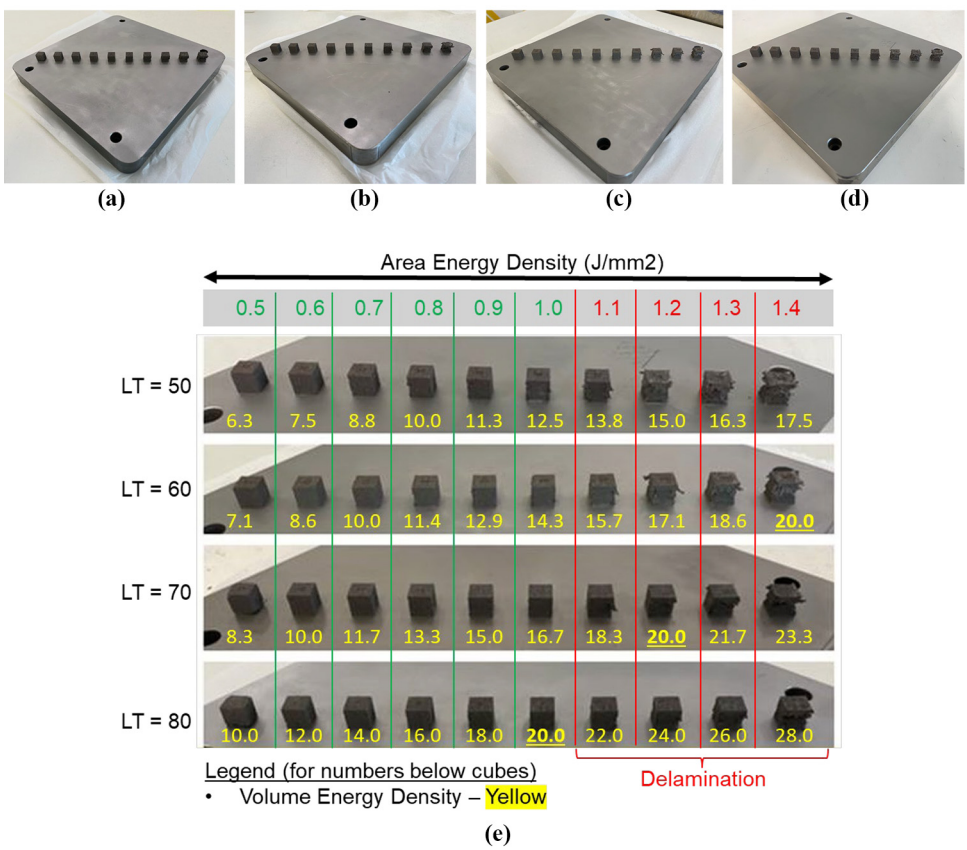

Notes: (a) Layer thickness (LT) = 50 µm (b) LT = 60 µm (c) LT = 70 µm (d) LT = 80 µm; (e) Overview
Source: Figure by authors

Figure 15 Outcome of phase II DoE highlighting the effects of layer thickness (T_L) and other process parameters

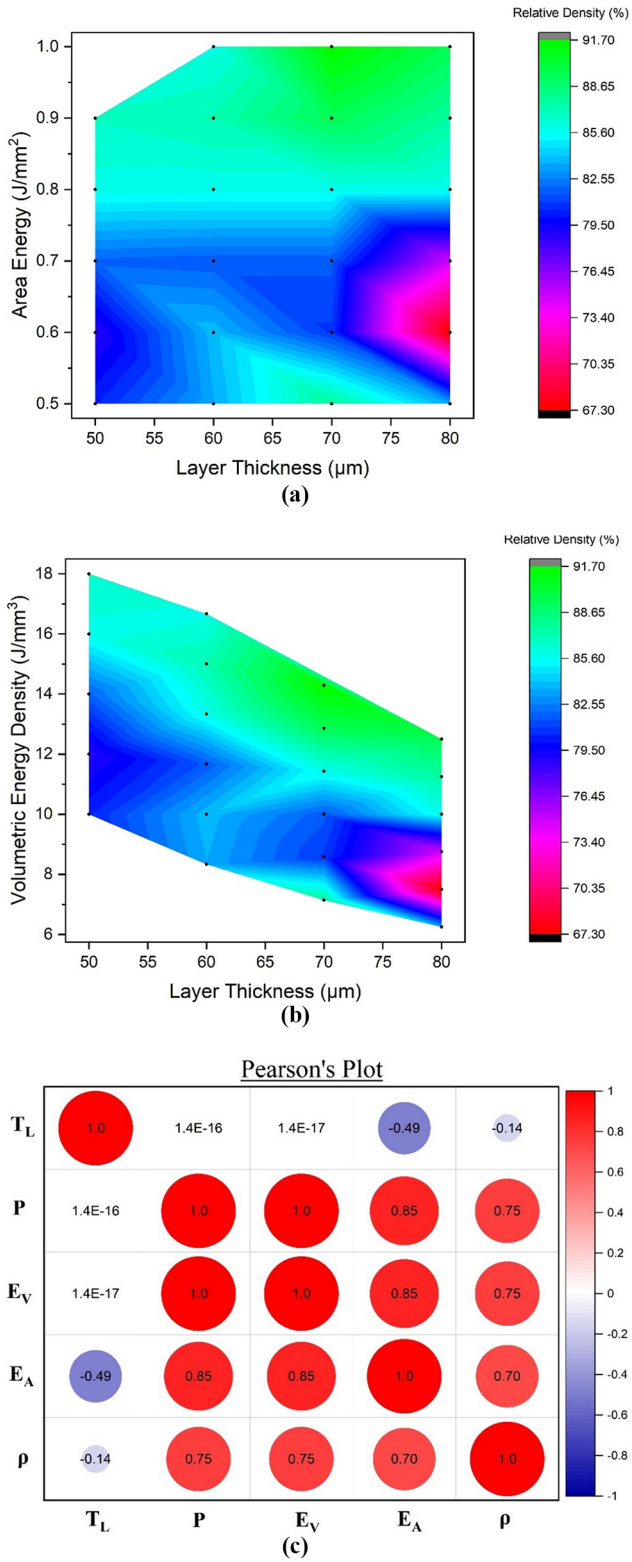

Notes: (a) EA; (b) EV; (c) Laser power (P), EV, EA and density of printed part (ρ)
Source: Figure by authors

Figure 16 The magnetic performance of the as received MQP-S (NdFeB) powder and the highest density LPBF NdFeB magnet of 92% relative density, measured using a SQUID-VSM

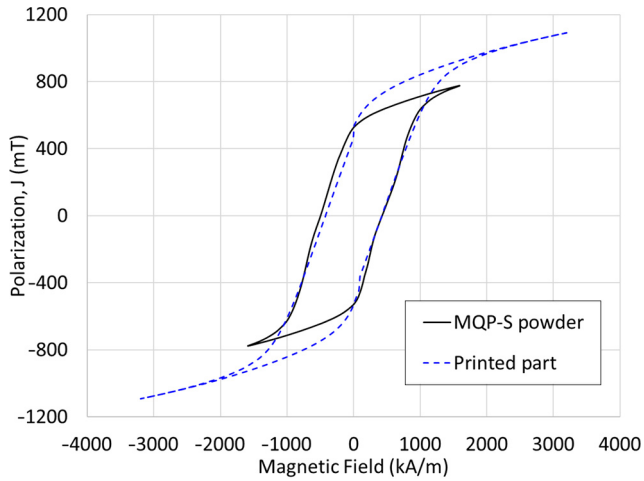

Source: Figure by authors

cubes printed using larger area energy density (typically above 1.0 J/mm^2) can be attributed to the process induced thermal residual stresses due to the rapid heating and cooling involved in LPBF processing.

4.4 Influence of process parameters on printed part properties

A total of 40 samples with visibly clear surfaces (free from delamination or cracks) were assessed for relative density by Archimedes density testing and the results are shown in Table 3. For each layer thickness, the relative density value was found to increase with an increase in the energy input as shown in Figure 17.

Measured using a SQUID-VSM, it was also found that the as received MQP-S (NdFeB) powder had a coercivity and remanence value of 558 kA/m and 528 mT respectively. On the other hand, the highest density LPBF NdFeB magnet had a coercivity and remanence value of 490 kA/m and 496 mT respectively. The hysteresis curves of both powder and part are shown in Figure 16 below.

Table 4 has two sections comparing results from this study against literature and the powder supplier's datasheet, with Section 1 on feedstock powder and Section 2 on printed specimens.

With regards to properties of printed specimen from this study and in literature, three different equipment were used: SQUID-VSM, PMG and Helmholtz coil w/fluxmeter (HCF). The magnetic properties of printed parts from this study was found to be similar to a study by (Huber *et al.*, 2019) where they have similarly used a SQUID-VSM. This study has yielded a slightly higher remanence but lower coercivity for the printed part, in comparison to the study by (Huber *et al.*, 2019). In comparison to studies by (N. Urban *et al.*, 2017a, 2017b, 2017c) and (Kolb *et al.*, 2016) where they both used a HCF for magnetic measurement, coercivity values were not available but the reported remanence was up to 13% higher than what was

Table 3 Results of density measurements conducted on coupons printed for DoE phase II (N.A. refers to defective prints), with highest achieved density in bold and underlined

S/N	Layer thickness (mm)	Laser power (W)	Scan speed (mm/s)	Hatch spacing (mm)	Area energy (J/mm^b)	Volumetric energy density (J/mm^3)	Relative density [a] (%)	Relative density [b] (%)
3.01	0.05	50	1000	0.1	0.5	10	79.48	80.45
3.02		60			0.6	12	77.86	78.81
3.03		70			0.7	14	80.92	81.91
3.04		80			0.8	16	84.80	85.84
3.05		90			0.9	18	85.65	86.70
3.06		100			1	20	86.90	87.97
3.07		110			1.1	22	89.66	90.76
3.08		120			1.2	24	N.A.	N.A.
3.09		130			1.3	26	N.A.	N.A.
3.10		140			1.4	28	N.A.	N.A.
4.01	0.06	50	1000	0.1	0.5	8.3	82.53	83.54
4.02		60			0.6	10	82.86	83.88
4.03		70			0.7	11.7	80.71	81.70
4.04		80			0.8	13.3	84.75	85.79
4.05		90			0.9	15	86.12	87.18
4.06		100			1	16.7	84.91	85.95
4.07		110			1.1	18.3	86.51	87.57
4.08		120			1.2	20	N.A.	N.A.
4.09		130			1.3	21.7	N.A.	N.A.
4.10		140			1.4	23.3	N.A.	N.A.
5.01	0.07	50	1000	0.1	0.5	7.1	86.76	87.82
5.02		60			0.6	8.6	79.93	80.91
5.03		70			0.7	10	80.71	81.70
5.04		80			0.8	11.4	84.75	85.79
5.05		90			0.9	12.9	88.38	89.46
5.06		100			1	14.3	90.55	*91.66*
5.07		110			1.1	15.7	88.58	89.67
5.08		120			1.2	17.1	86.83	87.89
5.09		130			1.3	18.6	N.A.	N.A.
5.10		140			1.4	20	N.A.	N.A.
6.01	0.08	50	1000	0.1	0.5	6.3	82.53	83.54
6.02		60			0.6	7.5	66.55	67.37
6.03		70			0.7	8.8	73.84	74.75
6.04		80			0.8	10	84.67	85.71
6.05		90			0.9	11.3	86.56	87.62
6.06		100			1	12.5	88.40	89.48
6.07		110			1.1	13.8	88.58	89.67
6.08		120			1.2	15	88.29	89.37
6.09		130			1.3	16.3	N.A.	N.A.
6.10		140			1.4	17.5	N.A.	N.A.

Note: [a]Relative density compared to measured true density of 7.34 g/cm^3; [b]Relative density compared to measured theoretical density of 7.43 g/cm^3
Source: Table by authors

found in this study. When compared to studies by (Bittner *et al.*, 2020; Bittner *et al.*, 2021) where they have used the PMG, the remanence and coercivity values were respectively 27% and 90% higher than what was found from this study. This study represents the first successful attempt in finding a suitable processing window for as received NdFeB powder with a measured size range of between 17 and 68 μm.

To demonstrate that the derived set of process parameters (Layer Thickness = 70 μm, Laser Power = 100 W, Scan Speed = 1000 mm/s, Hatch Spacing = 0.1 mm, Area Energy Density = 1.00 J/mm^2, Volumetric Energy Density = 14.3 J/mm^3) for the as received powder was useful for printing of prototypes, large hollow cylindrical samples were also printed (as shown in Figure 7).

4.5 Effect of heat treatment and magnetic annealing on the printed parts

To enhance the magnetic properties of LPBF-processed NdFeB magnets, heat treatment and subsequent annealing in a MVAO were performed. Initially, the magnets had an Archimedes density of 92%, coercivity of 490 kA/m and remanence of 496 mT. The first treatment involved heating to 1100°C at a rate of 11°C/min and holding for 2 h, increasing density to 96% but

Figure 17 Hollow cylindrical NdFeB samples printed using derived set of optimal parameters for as received powder

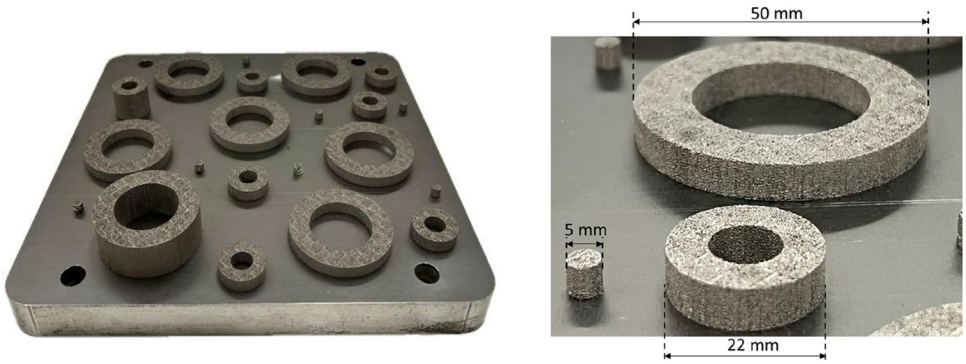

Notes: (a) Overview of print (b) Close-up image with dimensions
Source: Figure by authors

initially reducing coercivity due to grain growth. Subsequent furnace cooling to 600°C for 4 h relieved internal stresses, recovering coercivity. Quenching to room temperature in argon introduced internal stresses, enhancing coercivity, while EDM part removal caused minor reductions in both coercivity and remanence.

After these treatments, the magnets achieved a coercivity of 540 kA/m and remanence of 520 mT. Further magnetic annealing at 350°C for 4 h with a 1T magnetic field increased coercivity to 582 kA/m and remanence to 544 mT. This process relieved internal stresses and improved magnetic domain alignment.

In summary, the combined heat treatment and magnetic annealing significantly improved the magnetic properties of the LPBF-processed NdFeB magnets, with enhanced coercivity and remanence, albeit with some surface oxidation. Further refinement of the heat treatment process may be required to mitigate oxidation.

5. Conclusions and recommendations

This study presents a comprehensive investigation into the feasibility, optimization and enhancement of NdFeB magnets processed via LPBF. The primary conclusions derived from this research are:

- *Minimum Linear Energy Density:* Continuous track formation requires a minimum linear energy density of 0.10 J/mm.
- *Hatch Spacing Optimization:* A hatch spacing of 0.10 mm, with approximately 42% overlap, is critical to minimizing layer defects for layer thicknesses between 30 and 80 μm.
- *Stable Processing Window:* A stable area energy density (E_A) range of 0.6–1.0 J/mm^2 ensures consistent cuboid formation, although higher energy densities risk discontinuities due to insufficient fusion.
- *Maximizing Part Density:* Volumetric energy density (E_V) positively correlates with part density within the stable E_A range, achieving densities of up to 92%.
- *Improved Magnetic Properties via Post-Processing:* Heat treatment and magnetic annealing significantly enhanced magnetic properties, increasing density to 96%, coercivity to 582 kA/m and remanence to 544 mT.

5.1 Practical implications

The study demonstrates the effective use of as-received NdFeB powder with a particle size range of 17–68 μm, bypassing the need for costly sieving. Optimized LPBF parameters and post-processing protocols enable the production of high-quality 3D-printed NdFeB magnets, reducing material wastage and processing costs.

5.2 Future work

Further research should focus on refining LPBF parameters and post-processing methods to enhance magnetic and structural properties. Investigations into advanced annealing techniques and integration of these magnets into functional applications are recommended to broaden their industrial utility.

Acknowledgment

The authors gratefully acknowledge the funding support from Advanced Remanufacturing Technology Centre (ARTC), Singapore and National University Singapore. Yong Rong acknowledges the financial support from A*STAR Graduate Academy (AGA), Singapore in the form of an Engineering Doctorate (EngD) scholarship.

Declaration of competing interest

The authors declare that they have no known competing financial interests or personal relationships that could have appeared to influence the work reported in this paper.

Data availability

The data that support the findings of this study are available from the first author upon request.

Table 4 Comparison against optimized reported values for printed part density and magnetic performance

S/N	Title	Year	Powder condition	Layer Thickness (μm)	Specimen/ geometry	Volumetric energy density (J/mm^3)	Relative density (%)	Coercivity, H_{ci} (kA/m)	Remanence, B_r (mT)	Magnet testing equipment
Feedstock powder (MQP-S NdFeB powder)										
1	This study – feedstock powder (MQP-S NdFeB powder)	2024	Original condition					558	528	SQUID-VSM
3	Laser powder bed fusion of Nd–Fe–B permanent magnets (Bittner *et al.*, 2020)	2020	Sieved <40 μm					705	710	Permeagraph (magnetphysik GmbH)
4	Powder supplier datasheet (magnequench)	*Not stated*	Original condition					670–750	730–760	*Not stated*
Printed specimen										
5	This study – printed part (Highest density)	2024	As received (17–68 μm)	70	10 mm cube	14.30	92	490	496	SQUID-VSM
6	This study – printed part (Highest density, post-heat treatment)	2024	As received (17–68 μm)	70	5 mm cylinder	14.30	96	540	520	SQUID-VSM
7	This study – printed part (Highest density, post-heat treatment and post-magnetic annealing)	2024	As received (17–68 μm)	70	5 mm cylinder	14.30	96	582	544	SQUID-VSM
8	Laser Beam Melting of NdFeB for the production of Rare-Earth Magnets (Kolb *et al.*, 2016)	2016	Sieved <32 μm	20			86	N.A.	510	Helmholtz coil w/ fluxmeter
9	Net shape 3D printed NdFeB permanent magnet (Jaćim Jaćimović, 2017)	2016	Not stated	20	5 mm cube		92	695	590	Pulsed field magnetometer
10	Influences of process parameters on Rare Earth Magnets produced by Laser Beam Melting (N. Urban *et al.*, 2017a, 2017b, 2017c)	2017	Sieved <32 μm	20	5 mm cube	75.00	97	N.A.	560	Helmholtz coil w/ fluxmeter
11	Coercivity enhancement of selective laser sintered NdFeB magnets by grain boundary infiltration (Huber *et al.*, 2019)	2019	Infiltrated with low-melting point eutectic alloys	20		*(Derived stable window: 0.14 and 0.21)*		521 *(converted from 0.653T)*	436	SQUID-VSM
12	Laser powder bed fusion of Nd–Fe–B permanent magnets (Bittner *et al.*, 2020)	2020	Sieved <40 μm	30	5 mm cylinder	*(Derived stable window: 26.67–76.67)*	90	886	630	Permeagraph (magnetphysik GmbH)
13	Microstructure and magnetic properties of Nd-Fe-B permanent magnets produced by laser powder bed fusion (Bittner *et al.*, 2021)	2021	Sieved <40 μm	30		*(Derived stable window: 16.67–80.00)*	N.A.	921	630	Permeagraph (magnetphysik GmbH)

Source: Table by authors

References

Bittner, F., Thielsch, J. and Drossel, W.-G. (2020), "Laser powder bed fusion of Nd–Fe–B permanent magnets", *Progress in Additive Manufacturing*, Vol. 5 No. 1, pp. 3-9.

Bittner, F., Thielsch, J. and Drossel, W.-G. (2021), "Microstructure and magnetic properties of Nd-Fe-B permanent magnets produced by laser powder bed fusion", *Scripta Materialia*, Vol. 201, p. 113921.

Brown, D., Ma, B.-M. and Chen, Z. (2002), "Developments in the processing and properties of NdFeb-type permanent magnets", *Journal of Magnetism and Magnetic Materials*, Vol. 248 No. 3, pp. 432-440.

Buhairi, M.A., Foudzi, F.M., Jamhari, F.I., Sulong, A.B., Radzuan, N.A.M., Muhamad, N., Mohamed, I.F., Azman, A.H., Harun, W.S.W. and Al-Furjan, M. (2022), "Review on volumetric energy density: influence on morphology and mechanical properties of Ti6Al4V manufactured via laser powder bed fusion", *Progress in Additive Manufacturing*, Vol. 8 No. 2, pp. 1-19.

Caiazzo, F., Alfieri, V. and Casalino, G. (2020), "On the relevance of volumetric energy density in the investigation of inconel 718 laser powder bed fusion", *Materials*, Vol. 13 No. 3, p. 538.

Chan, Y.R., Seetharaman, S., Fuh, J.Y. and Lee, H.P. (2024), "Advancing neodymium permanent magnets with laser powder bed fusion technology: a comprehensive review of process-structure-property relationship", *Materials Advances*, Vol. 5 No. 22.

Chen, Q., Taylor, H., Takezawa, A., Liang, X., Jimenez, X., Wicker, R. and To, A.C. (2021), "Island scanning pattern optimization for residual deformation mitigation in laser powder bed fusion via sequential inherent strain method and sensitivity analysis", *Additive Manufacturing*, Vol. 46, p. 102116.

Cheng, B., Shrestha, S. and Chou, K. (2016), "Stress and deformation evaluations of scanning strategy effect in selective laser melting", *Additive Manufacturing*, Vol. 12, pp. 240-251.

Echlin, P. (2011), *Handbook of Sample Preparation for Scanning Electron Microscopy and X-Ray Microanalysis*, Springer Science & Business Media, New York, NY.

El-Sayegh, S., Romdhane, L. and Manjikian, S. (2020), "A critical review of 3D printing in construction: benefits, challenges, and risks", *Archives of Civil and Mechanical Engineering*, Vol. 20 No. 2, pp. 1-25.

Emminghaus, N., Hoff, C., Hermsdorf, J. and Kaierle, S. (2020), "Laser powder bed fusion of NdFeB and influence of heat treatment on microstructure and crack development", *Procedia CIRP*, Vol. 94, pp. 211-216.

Ferretti, L. (2017), "Virtual design and optimization of PM motors for application to an electric vehicle".

Filip, O., Hermann, R., Gerbeth, G., Priede, J. and Biswas, K. (2005), "Controlling melt convection–an innovation potential for concerted microstructure evolution of Nd-Fe-B alloys", *Materials Science and Engineering: A*, Vols. 413/414, pp. 302-305.

Franke, T.K., Florian, H., Basri, A., Christoph, D., Nikolaus, U., Dominik, M. and Jörg, L. (2016), "Laser beam melting of NdFeB for the production of rare-earth magnets", IEEE, available at: https://ieeexplore.ieee.org/document/7851311

Fukuno, A., Hirose, K. and Yoneyama, T. (1990), "Coercivity mechanism of sintered NdFeB magnets having high coercivities", *Journal of Applied Physics*, Vol. 67 No. 9, pp. 4750-4752.

Goll, D., Trauter, F., Bernthaler, T., Schanz, J., Riegel, H. and Schneider, G. (2021), "Additive manufacturing of bulk nanocrystalline FeNdB based permanent magnets [article", *Micromachines*, Vol. 12 No. 5, p. 538, doi: 10.3390/mi12050538.

Honshima, M. and Ohashi, K. (1994), "High-energy NdFeB magnets and their applications", *Journal of Materials Engineering and Performance*, Vol. 3 No. 2, pp. 218-222.

Huber, C., Sepehri-Amin, H., Goertler, M., Groenefeld, M., Teliban, I., Hono, K. and Suess, D. (2019), "Coercivity enhancement of selective laser sintered NdFeB magnets by grain boundary infiltration", *Acta Materialia*, Vol. 172, pp. 66-71.

Huijuan Liu, S.T.Z.Z.W.H. (2019), "Multi-Objective optimization design and performance comparison of permanent magnet synchronous motor for EVs based on FEA", *IET Electric Power Applications*, Vol. 13 No. 8, doi: 10.1049/iet-epa.2019.0069.

Jaćim Jaćimović, F.B.L.G.H.F.G.J.G.M.C.T.T.R.A.S. (2017), "Net shape 3D printed NdFeB permanent magnet", *Advanced Engineering Materials*, Vol. 19 No. 8, doi: 10.1002/adem.201700098.

Jacimovic, J., Binda, F., Herrmann, L.G., Greuter, F., Genta, J., Calvo, M., Tomse, T. and Simon, R.A. (2017), "Net shape 3D printed NdFeB permanent magnet [article]", *Advanced Engineering Materials*, Vol. 19 No. 8, p. 7, doi: 10.1002/adem.201700098. Article 1700098

Jacimovic, J., Christen, T. and Denervaud, E. (2020), "Self-organized giant magnetic structures via additive manufacturing in NdFeB permanent magnets [article]", *Additive Manufacturing*, Vol. 34, p. 7, doi: 10.1016/j.addma.2020.101288. Article 101288

Kolb, T., Huber, F., Akbulut, B., Donocik, C., Urban, N., Maurer, D. and Franke, J. (2016), "Laser beam melting of NdFeB for the production of rare-earth magnets", *2016 6th International Electric Drives Production Conference (EDPC)*.

Kruth, J.-P., Badrossamay, M., Yasa, E., Deckers, J., Thijs, L. and Van Humbeeck, J. (2010), "Part and material properties in selective laser melting of metals", *Proceedings of the 16th International Symposium on Electromachining (ISEM XVI)*,

Liu, B., Wildman, R., Tuck, C., Ashcroft, I. and Hague, R. (2011), "Investigation the effect of particle size distribution on processing parameters optimisation in selective laser melting process", *2011 International solid freeform fabrication symposium, magnequench. MQP-S-11-9-20001 powder datasheet*, available at: https://mqitechnology.com/product/mqp-s-11-9-20001/

Mellin, P., Jönsson, C., Åkermo, M., Fernberg, P., Nordenberg, E., Brodin, H. and Strondl, A. (2016), "Nano-sized by-products from metal 3D printing, composite manufacturing and fabric production", *Journal of Cleaner Production*, Vol. 139, pp. 1224-133.

Rafal Wrobel, B.M. (2019), "Additive manufacturing in construction of electrical machines – a review", available at: https://ieeexplore.ieee.org/document/8887765/authors#authors

Ravikumar, S., Surekha, R. and Thavarajah, R. (2014), "Mounting media: an overview", *Journal of Dr. NTR University of Health Sciences*, Vol. 3 No. 5, pp. S1-S8.

Stopic, S. and Friedrich, B. (2021), "Advances in understanding of the application of unit operations in metallurgy of rare earth elements [review", *Metals*, Vol. 11 No. 6, p. 20, Article 978, doi: 10.3390/met11060978.

Urban, N., Huber, F. and Franke, J. (2017a), "Influences of process parameters on rare earth magnets produced by laser beam melting", 2017 7th International Electric Drives Production Conference (EDPC).

Urban, N., Huber, F., Franke, J. and Ieee, M. (2017b), "Influences of process parameters on rare earth magnets produced by laser beam melting", *International Electric Drives Production Conference [2017 7th international electric drives production conference (edpc)]. 7th International Electric Drives Production Conference (EDPC)*, *Wuerzburg*.

Urban, N., Meyer, A., Kreitlein, S., Leicht, F. and Franke, J. (2017c), "Efficient near net shape production of high energy rare earth magnets by laser beam melting", *Applied Mechanics and Materials*, Vol. 871.

Vock, S., Klöden, B., Kirchner, A., Weißgärber, T. and Kieback, B. (2019), "Powders for powder bed fusion: a review", *Progress in Additive Manufacturing*, Vol. 4 No. 4, pp. 383-397.

Watring, D.S., Benzing, J.T., Hrabe, N. and Spear, A.D. (2020), "Effects of laser-energy density and build orientation on the structure–property relationships in as-built inconel 718 manufactured by laser powder bed fusion", *Additive Manufacturing*, Vol. 36, p. 101425.

Wu, J.L., Aboulkhair, N.T., Degano, M., Ashcroft, I. and Hague, R.J.M. (2021), "Process-structure-property relationships in laser powder bed fusion of permanent magnetic Nd-Fe-B [article]", *Materials & Design*, Vol. 209, p. 11, doi: 10.1016/j.matdes.2021.109992.

Yan, G.H., Chen, R.J., Ding, Y., Guo, S., Lee, D. and Yan, A. (2011), "The preparation of sintered NdFeB magnet with high-coercivity and high temperature-stability", *Journal of Physics: Conference Series*, Vol. 266.

Yasa, E., Deckers, J., Craeghs, T., Badrossamay, M. and Kruth, J.-P. (2009), "Investigation on occurrence of elevated edges in selective laser melting", *2009 International Solid Freeform Fabrication Symposium*.

Yong, J.Z. and Lu, Y. (2003), "Optimum design of magnet shape in permanent-magnet synchronous motors", IEEE, available at: https://ieeexplore.ieee.org/abstract/document/1252828

Yu, K.-S., Cheng, C.-W., Lee, A.-C., Jian, W.-Y.J., Chang, W.-C., Chang, T.-W. and Tsai, M.-C. (2022), "Additive manufacturing of NdFeB magnets by synchronized three-beam laser powder bed fusion", *Optics & Laser Technology*, Vol. 146, p. 107604.

About the authors

Yong Rong Chan from National University of Singapore (NUS), in 2020, and is currently pursuing a Doctor of Engineerin 2016, where he focuses on additive manufacturing (AM) feedstock characterization and investigation of AM process optimization for metallic materials. He earned his BE in Mechanical Engineering from the National University of Singapore (NUS), in 2020, and is currently pursuing a Doctor of Engineering (EngD) at NUS. Yong Rong Chan is the corresponding author and can be contacted at: chan_yong_rong@hotmail.com

Sankaranarayanan Seetharaman is a Senior Scientist at the Advanced Remanufacturing Technology Centre in Singapore, where he focuses on investigating process-structure-property relationships in metallic materials. He earned his BE in Mechanical Engineering from Anna University, India, in 2007, and completed his PhD at the National University of Singapore (NUS) in 2014. Prior to joining ARTC, he was a Senior Application Engineer at ANSYS Inc., India, from 2018 to 2020 providing valuable technical support for additive manufacturing simulation activities. A professional member of The Minerals, Metals and Materials Society, Seetharaman is an active contributor to the Light Metals Division. He has an extensive publication record with over 50 research articles in peer-reviewed journals and conference proceedings, amassing more than 1,500 citations. His current h-index is 25, and i-10 index is 42.

Jerry Y.H. Fuh is a Professor at the Department of Mechanical Engineering, National University of Singapore (NUS) and the Founding Director and Advisor of NUS Centre for Additive Manufacturing (AM.NUS), Singapore. He is a Fellow of SME and ASME, USA and a PE from California, USA. Prof. Fuh has devoted himself to the research of Additive Manufacturing (AM) processes or 3D Printing (3DP) since 1995. He and his colleagues have established the NUS's cross-faculty R&D programme focusing on AM/3DP-enabled biomedical applications and set up SGD$20M+ advanced AM laboratories through several Singapore agencies' and University grants.

Heow Pueh Lee is a Provost's Chair Professor at the Department of Mechanical Engineering, National University of Singapore. He obtained his Bachelor degree from the University of Cambridge, Master of Engineering from the National University of Singapore, Master of Science and PhD from Stanford University. His research interests include acoustic and vibration, modeling and simulations and additive manufacturing. His is an Associate Editor for Applied Acoustics (Elsevier), and Member of Editorial Board for Acta Mechanica Sinica,*International Journal of Applied Mechanics*, *and Scientific Reports*.